

Dynamical MJO forecasts using an ensemble subseasonal-to-seasonal forecast system of the IAP-CAS model

Yangke Liu^{1,6}, Qing Bao^{*1}, Bian He¹, Xiaofei Wu², Jing Yang³, Yimin Liu¹, Guoxiong Wu¹, Tao Zhu¹, Siyuan Zhou¹, Yao Tang^{1,6}, Ankang Qu^{1,7}, Yalan Fan³, Anling Liu³, Dandan Chen^{1,6}, Zhaoming Luo^{1,7}, Xing Hu⁴, Tongwen Wu⁵

¹State Key Laboratory of Numerical Modeling for Atmospheric Sciences and Geophysical Fluid Dynamics (LASG), Institute of Atmospheric Physics, Chinese Academy of Sciences, Beijing 100029, China

²School of Atmospheric Sciences/Plateau Atmosphere and Environment Key Laboratory of Sichuan Province, Chengdu University of Information Technology, Chengdu 610225, China

³Faculty of Geographical Science, Beijing Normal University, Beijing 100875, China

⁴National Meteorological Information Center, China Meteorological Administration, Beijing 100081, China

⁵Center for Earth System Modeling and Prediction, China Meteorological Administration, Beijing 100081, China

⁶College of Earth and Planetary Sciences, University of Chinese Academy of Science, Beijing 100049, China

⁷School of Emergency Management Science and Engineering, University of Chinese Academy of Science, Beijing 100049, China

Correspondence to: Qing Bao (baoqing@mail.iap.ac.cn)

17 **Abstract.** The Madden-Julian Oscillation (MJO) is a crucial predictability source on a sub-seasonal to seasonal (S2S) timescale.
18 Therefore, the models participating in the WWRP/WCRP S2S prediction project focus on accurately predicting and analyzing
19 the MJO. This study provided a detailed description of the configuration within the IAP-CAS S2S forecast system. We assessed
20 the accuracy of the IAP-CAS model's MJO forecast using traditional RMM analysis and cluster analysis. Then, we explained
21 the reasons behind any bias observed in the MJO forecast. Comparing the 20-year hindcast with observations, we found that
22 the IAP-CAS ensemble mean has a skill of 24 days. However, the ensemble spread still has potential for improvement. To
23 examine the MJO structure in detail, we used cluster analysis to classify the MJO events during boreal winter into four types:
24 fast-propagating, slow-propagating, standing, and jumping patterns of MJO. The model exhibits biases of overestimated
25 amplitude and faster propagation speed in the propagating MJO events. Upon further analysis, it was found that the model
26 forecasted a wetter background state. This leads to more intense forecasted convection and stronger coupled waveswinds,
27 especially in the fast MJO events. ~~However, the horizontal moisture advection effect for eastward propagation is overestimated~~
28 ~~in IAP-CAS due to the wetter state and more substantial MJO circulations, which results in a faster MJO mode. The~~
29 ~~overestimation of the strength and length of MJO-coupled waves results in a accelerated MJO mode and faster dissipation in~~
30 ~~the IAP-CAS model.~~ These findings show that the IAP-CAS skilfully forecasts signals of MJO and its propagation, and they
31 also provide valuable guidance for improving the current MJO forecast by developing the ensemble system and moisture
32 forecast.

33 **Keywords:** MJO prediction, S2S, IAP-CAS, FGOALS-f2, Cluster Analysis

34 1 Introduction

35 With the increasing occurrence of metrological disasters in recent years, there has been growing attention toward S2S forecast,
36 as it bridges the gap between weather and climate forecasts and reduces disaster risks through early warnings. In November
37 2013, the WWRP/WCRP S2S prediction project (Phase 1) was launched, with the principal objectives of enhancing S2S
38 forecast accuracy and advancing our comprehension of its dynamics and climate drivers. Then, work on the S2S research
39 continued in Phase 2, from 2018 to 2023. The whole project has made a significant contribution to the development of S2S
40 prediction.

41 MJO (Madden and Julian, 1971) is a crucial predictability source of S2S forecasts. It is a significant tropical oscillation with
42 a period of 30-60 days, characterized by expansive cloud masses and precipitation systems that propagate eastward along the
43 equatorial regions. Accurate S2S prediction requires a good representation of MJO. Many studies have clarified the relationship
44 between the MJO and global weather and climate, such as monsoons_(Goswami, 2012; Hsu, 2012; Lau and Chan, 1986;
45 Wheeler et al., 2009; Liu et al., 2022) ~~(Goswami, 2012; Hsu, 2012; Lau and Chan, 1986; Wheeler et al., 2009)~~, tropical cyclones
46 (Bessafi and Wheeler, 2006; Ferreira et al., 1996; Hall et al., 2001) and El Niño-Southern Oscillation (ENSO; Lau et al., 2005;
47 Zhang, 2005). The convective and circulation anomalies associated with MJO establish intricate connections across global
48 weather and climate systems on the S2S timescale. Being able to accurately forecast the MJO can have a positive impact on
49 the forecast of other related systems (Cassou, 2008; Vitart and Molteni, 2010; Wu et al., 2007). Achieving an accurate forecast
50 of MJO becomes a primary objective in the field of S2S forecasts.

51 With an enhanced comprehension of the underlying physical mechanisms governing the MJO and the continuous improvement
52 of numerical models, remarkable advancements have been achieved in the MJO forecast. In Coupled Model Intercomparison
53 Project Phase 6 (CMIP6), models that exhibited lower forecast skills (Hung et al., 2013) in Coupled Model Intercomparison
54 Project Phase 5 (CMIP5) have demonstrated noteworthy improvements in the simulation of MJO (Ahn et al., 2020). Generally,
55 the models in CMIP6 simulate more realistic eastward propagation and precipitation over the Maritime Continent (MC) region
56 (Ahn et al., 2019; Chen et al., 2022).

57 However, for S2S forecasts, the improvement of model physics is one aspect of advancing S2S forecasts, as various factors
58 impact MJO forecast skills, such as initialization and ensemble generation (Kim et al., 2018). The forecast skills of the MJO
59 in most models is typically 3-4 weeks (Vitart, 2017), while the estimate of predictability of MJO is approximately 5-7 weeks
60 (Waliser et al., 2003; Neena et al., 2014). These facts underscore the persisting challenges in the S2S forecasts.

61 The realistic forecast of MJO eastward propagation is one of the challenges repeatedly mentioned in recent years (Jiang, 2017;
62 Kim, 2019; Lim et al., 2018; Wang and Lee, 2017). The MJO propagation skill is closely related to the forecast of the state in
63 the Maritime Continent (MC) region (Gonzalez and Jiang, 2017). Many studies have pointed out the "MC barrier" (Hendon
64 and Salby, 1994; Rui and Wang, 1990a; Vitart et al., 2017) during the MJO's propagation through the MC region. The "MC

65 barrier" refers to a notable deterioration of the MJO signal when it traverses the MC area, but this phenomenon is usually
66 amplified in the climate models (Kim et al., 2014b; Neena et al., 2014; Xiang et al., 2022, 2015), showing the model's limitation
67 in preserving MJO propagation within the MC region. The moisture mode theory (Raymond and Fuchs, 2009) has been
68 proposed to explain this phenomenon. It suggests that the advection of seasonal mean moisture by the MJO-related circulation
69 anomalies in the lower troposphere is crucial to MJO's propagation through the MC region (Jiang, 2017; Kim, 2019). In models
70 that are hard to capture the realistic propagation of MJO, the mean low-troposphere moisture amplitude over the MC is
71 underestimated, resulting in a weakened horizontal moisture gradient (Gonzalez and Jiang, 2017; Kim, 2017). This discrepancy
72 in moisture advection hinders MJO propagation.

73 The Institute of Atmospheric Physics at the Chinese Academy of Sciences (IAP-CAS) has been actively involved in climate
74 model development and applications since the CMIP1 in the 1990s. As for the IAP-CAS model, it has already shown a
75 significant enhancement in MJO simulation in CMIP6 compared to CMIP5 (Chen et al., 2022), but the performance of the
76 S2S system in IAP-CAS remains uncertain and requires comprehensive evaluation. Therefore, the objectives of this article are
77 fourfold: Firstly, the aim is to introduce the S2S forecast system of the IAP-CAS model. Secondly, to evaluate the forecast
78 skills of the IAP-CAS in the MJO forecast. Thirdly, the aim is to analyze the evaluation results to identify the sources of
79 forecast errors. This will facilitate further improvements in the MJO forecast. At last, we hope that the verification and analysis
80 process can provide some valuable insights for other models.

81 The structure of the paper is as follows. A thorough review of the IAP-CAS model and S2S ensemble forecast system is
82 introduced in Section 2. Section 3 describes the observation data and primary methodology utilized in the article. Section 4
83 assesses the overall MJO forecast skills in IAP-CAS. Section 5 focuses on analyzing the propagation details of the
84 fast-propagating and slow-propagating MJO. After that, in Section 6, we discuss the potential causes of any bias observed
85 in the MJO forecast. In Section 7, we summarize our findings and have a discussion.

86 **2 The global S2S ensemble forecast system of IAP-CAS**

87 The architecture of the IAP-CAS S2S ensemble forecast system is depicted in Figure 1. In this section, we will give a thorough
88 description of the S2S system, covering the model, initialization methods, ensemble generation approaches, and the resulting
89 datasets.

90 **2.1 Configuration of IAP-CAS model**

91 The climate system model CAS FGOALS-f2 (The Flexible Global Ocean-Atmosphere-Land System model Finite Volume
92 version 2, Chinese Academy of Sciences; Bao 2019; Bao et al. 2020) is the core of the IAP-CAS S2S ensemble forecast system.
93 It is developed by the State Key Laboratory of Numerical Modeling for Atmospheric Sciences and Geophysical Fluid

94 Dynamics (LASG) at the Institute of Atmospheric Physics (IAP), Chinese Academy of Sciences (CAS). We utilize the
95 institution name, IAP-CAS, as a proxy for the model.

96 FGOALS-f2 is a fully coupled model that encompasses four components: atmospheric, land, oceanic, and sea ice models, with
97 its configuration detailed in Table 1. The atmospheric component is version 2 of the Finite-volume Atmospheric Model
98 (FAMIL2; Li et al. 2019), with a standard horizontal resolution of C96, which means 96×96 grid points in each tile of the
99 cube sphere, roughly equivalent to 1-degree resolution. Vertically, it features 32 hybrid sigma-pressure levels, with the
100 uppermost level situated at 1 hPa (The Hybrid coefficients are listed in Table [A12](#)). The land surface component used in
101 FGOALS-f2 is version 4 of the Community Land Model (CLM4.0; Oleson et al. 2010; Lawrence et al. 2011), featuring a
102 horizontal resolution nearly at 1-degree resolution. The oceanic component is Parallel Ocean Program version 2 (POP2;
103 Kerbyson and Jones 2005), which utilizes a displaced-pole grid with the North Pole shifted to Greenland. This grid has a
104 resolution of gx1v6, approximately equivalent to a 1-degree horizontal resolution, and includes 60 vertical layers. The sea ice
105 component is the Los Alamos Sea Ice Model version 4.0 (CICE4; Hunke et al. 2010), sharing the exact horizontal resolution
106 as the ocean model. These four components are coupled via the coupler version 7 in the Community Earth System Model
107 (CESM; Craig et al. 2012).

108 It is worth noting that FAMIL2, the latest generation atmospheric model from LASG, has adopted the Finite-Volume Cubed-
109 Sphere Dynamical Core (FV3; Lin 2004; Putman and Lin 2007) as its dynamical core. FV3 solves the fully compressible Euler
110 equations on the gnomonic cubed-sphere grid and a Lagrangian vertical coordinate. Fast vertically propagating sound and
111 gravity waves are solved by the semi-implicit method (Harris et al., 2020). This enhancement of the atmospheric component
112 results in improved computational efficiency and accuracy. Besides, the key parameterization in FAMIL2 is a Resolved
113 Convection Precipitation scheme (RCP), which is independently developed to calculate the microphysics processes in the
114 convective precipitation for both deep and shallow convection (Bao and Li, 2020). Due to the rapid phase changes occurring
115 within the convective cloud, a sub-time step of 150 seconds is employed for the calculation of microphysical processes within
116 a physical timestep of 30 minutes. FAMIL2 has also implemented the University of Washington Moist Turbulence
117 parameterization scheme (UWMT, Park and Bretherton 2009) as its boundary layer scheme. The microphysical
118 parameterization used in FAMIL2 is the revised Lin scheme, which is a single-moment scheme (Zhou et al., 2019).

119 ~~Building upon previous work, it has been observed that the IAP-CAS model can effectively reproduce the patterns and intensity
120 of ENSO variability (Fig. A2), and it also shows a skillful forecast of tropical cyclones (Li et al., 2021, 2022). As mentioned
121 in Section 1, the activity of the MJO is significantly impacted by the tropical weather and climate systems, including ENSO
122 and tropical cyclones (TCs). The accurate forecast of ENSO and TCs heightens our anticipation for MJO forecast skill in the
123 IAP-CAS model. FAMIL2 has already provided a realistic forecast of convectively coupled equatorial waves (CCEWs) and
124 MJO convection (Li et al., 2019). The S2S forecast system also exhibits excellent performance in forecasting arctic sea ice
125 (Liu et al., 2023) and spring rainfall (Fan et al., 2023).~~

126 2.2 Initialization scheme of the S2S forecast system

127 The S2S forecast system of the IAP-CAS model adopts a Newtonian nudging method with time-varying treatment (Jeuken et
 128 al., 1996) to complete the initialization of the atmosphere and ocean. The reanalysis nudging and the forecast nudging are the
 129 two components that make up the initialization process, which is seen in Figure 2. Table 3-A2 provides a summary of the
 130 detailed technical specifics for these two nudging processes.

131 The reanalysis nudging initializes the atmospheric variables, including temperature, surface pressure, sea level pressure, and
 132 surface wind from the NCEP Final Operational Global Analysis datasets (FNL, <http://rda.ucar.edu/datasets/ds083.2>,
 133 ds083.2|DOI: 10.5065/D6M043C6). The oceanic variable of potential temperature from the National Oceanic and Atmospheric
 134 Administration (NOAA) Optimum Interpolation Sea Surface Temperature (OISST) reanalysis data (Reynolds et al., 2007) is
 135 also included. These reanalysis data serve as observations in the eq. (1) to diminish errors in the initial condition:

$$136 \quad x(t) = x_{model}(t) + N_{rea}(t)[x_{obs}(t) - x_{model}(t)] \quad (1)$$

137 where t is the time, $x(t)$ is the field after nudging process, $x_{model}(t)$ represents the model forcing, $x_{obs}(t)$ represents the
 138 “truth” value, and $N_{rea}(t)$ is a relaxation coefficient that varies over time, which constantly adjusts the model results during
 139 the integration process, making it approximate to the observed values while being constrained by the dynamical constraints of
 140 the physical model. The calculation process for $N_{rea}(t)$ is as follows:

$$141 \quad N_{rea}(t) = \frac{\Delta t}{\frac{T}{1+c} \frac{e^{\frac{t\%T}{T}} + \Delta t}{(2\pi \frac{t\%T}{T})}} \quad (2)$$

142 Δt is the time step in FAMIL2, which is 0.5h for C96 resolution (approximately 1-degree resolution). T represents the time
 143 window with a value of 6 hours. As depicted in Figure 2a, the relaxation coefficient varies as a cosine function. It is large at
 144 the beginning and end of the temporal window, thereby facilitating accelerated convergence of the model results towards
 145 observations. While in the middle of the time window, N_{rea} becomes smaller and even drops to zero, which indicates the
 146 reliability of the reanalysis data decreases. The reason is that the reanalysis data within the time window is obtained through
 147 interpolation between its start and end values.

148 In the forecast nudging, the initialization process adheres to a similar nudging algorithm at 6-h intervals, as shown in eq. (3).

$$149 \quad x(t) = x_{model}(t) + N_{fcst}(t)[x_{fcst}(t) - x_{model}(t)] \quad (3)$$

150 Nevertheless, the atmospheric variables assimilated into the S2S system are sourced from the GFS weather forecast, denoted
 151 as $x_{fcst}(t)$. The relaxation coefficient $N_{fcst}(t)$ is as follows:

$$152 \quad N_{fcst}(t) = \frac{\Delta t}{\frac{T}{1+c} \frac{e^{\frac{t\%T}{T}} + \Delta t}{(2\pi \frac{t\%T}{T})}} \cdot \cos\left(\frac{\pi}{2} \cdot \frac{(t-t\%T)}{4mT}\right) \quad (4)$$

153 Compared to N_{rea} , N_{fcst} is multiplied by a decay factor, which also varies in accordance with the cosine function. In this
 154 context, the number of days for forecast nudging is denoted by m , and the system is configured with a 10-day forecast nudging
 155 period. Figure 2b illustrates the variation of N_{fcst} , which decreases as the reliability of weather forecast data diminishes over
 156 time, ultimately reaching zero by the 10th day.

157 In forecast nudging, we used 10 days of GFS weather forecast data for nudging. One purpose of this approach is to avoid
158 coupling shock at initialization. Additionally, we aim to enhance the quality of initial forecasts in S2S by nudging GFS weather
159 forecast data to ultimately improve S2S prediction accuracy, as the skill of weather forecasts is higher than that of S2S forecasts
160 during the initial period.

161 Summarily, the S2S forecast system commences its daily forecast from the initial condition derived via reanalysis nudging. It
162 then fine-tunes the forecasts with weather prediction data through the forecast nudging process. This initialization system
163 effectively reduces system errors in the model and augments forecast accuracy.

164 **2.3 Time-lagged method for ensemble generation**

165 The value of ensemble forecasts in medium to long-term forecasts has been repeatedly emphasized (Liu, 2003; Vitart and
166 Molteni, 2009). In addition to improving the physical scheme of the model, devising an effective approach for ensemble
167 generation might have a considerable impact on the MJO forecast. The IAP-CAS S2S ensemble forecast system utilizes the
168 time-lagged method (Hoffman and Kalnay, 1983) to generate ensemble members.

169 A schematic diagram of the time-lagged method is depicted in Figure 2b. During the initial day of the forecast nudging, the
170 S2S system issues forecasts from 00Z, 06Z, 12Z, and 18Z, resulting in the generation of 4 ensemble members. The core idea
171 behind this approach is to introduce perturbations by leveraging lagged initialization times.

172 **2.4 Hindcast experiment and real-time forecast**

173 The S2S ensemble forecast system provides daily forecasts, forecasting weather and climate conditions for the upcoming 65
174 days. Out of the 65 days, 5 days are reserved for extending the ensemble members by using the time-lagged method, ensuring
175 a complete forecast for at least 60 days. Since June 1st, 2019, the IAP-CAS S2S system has been operating 16 ensemble
176 members daily for real-time forecasts. So far, approximately 8.2TB of real-time data has been uploaded to the S2S website.
177 For hindcast experiments from 1999 to 2018, the system has run 4 ensemble members daily, generating a dataset of
178 approximately 11TB.~~Since June 1st, 2019, the IAP-CAS S2S system has been operating 16 ensemble members daily for real-~~
179 ~~time forecast, and for hindcast experiments from 1999 to 2018, it has run 4 ensemble members daily.~~ Our subsequent research
180 is based on the 20-year hindcast experiment.

181 In 2021, the IAP-CAS model participated in phase II of the S2S Project (Vitart et al., 2017) successfully, providing the 20-
182 year hindcast and real-time forecast data generated by the S2S ensemble forecast system. Detailed information regarding the
183 data is listed in Table 4A3, and Table A45 shows the list of output variables. The output data is interpolated to a standardized
184 horizontal resolution of $1.5^{\circ} \times 1.5^{\circ}$, following the S2S's requirements, and is stored in version 2 of General Regularly-distributed
185 Information in Binary (GRIB2) format. The output data of the S2S system is publicly available on three S2S Data Portals
186 (ECMWF, CMA, and IRI).

187 3 Datasets and methods

188 3.1 datasets

189 The observational datasets used for the MJO verification include the NOAA daily outgoing longwave radiation (OLR;
190 Liebmann and Smith 1996), daily wind from the National Centers for Environmental Prediction (NCEP)/Department of Energy
191 (DOE) Reanalysis 2 dataset (Kanamitsu et al., 2002), daily specific humidity from ECMWF Reanalysis version 5 (ERA5;
192 ERA 2017), and the precipitation product from the Global Precipitation Climatology Project (GPCP; Adler et al. 2003). To
193 facilitate computation and meaningful comparisons, both observation and hindcast datasets have been uniformly interpolated
194 to a horizontal resolution of $2.5^\circ \times 2.5^\circ$. Seven pressure levels (1000, 925, 850, 700, 500, 300, and 200hPa) of wind and specific
195 humidity are extracted for analysis.

196 3.2 MJO RMM index

197 To conduct a quantitative assessment of MJO, we have employed the widely used Real-time Multivariate MJO (RMM) index
198 (Wheeler and Hendon, 2004a) to extract the MJO signal. This index consists of two components, RMM1 and RMM2, which
199 are the first and second principal components of the combined empirical orthogonal functions (EOFs) of multiple variables,
200 including OLR, 200hPa zonal wind (U200), and 850hPa zonal wind (U850). It serves as a tool for tracking the location and
201 amplitude characteristics of MJO.

202 The calculation of the RMM index refers to the method described in Gottschalck et al. (2010). Detailed calculation steps are
203 as follows:

- 204 1) Remove the 0-3 waves of the climatology and low-frequency variability of the U200, U850, and OLR variables from both
205 the observation and hindcast data. It is noteworthy that removing low-frequency variability is to subtract the mean of the
206 past 120 days from the anomalies. For model forecast, this is the mean model anomalies of the previous forecast days,
207 plus the mean observed anomalies of the remaining days.
- 208 2) Average the anomalies between 15° S and 15° N and normalize the three variables, using the pre-computed coefficients
209 as in Gottschalck et al. (2010).
- 210 3) Project the anomalies onto the observed combined EOF eigenvectors from Wheeler and Hendon (2004b) to get RMM1
211 and RMM2.

212 Bivariate anomaly correlation coefficient (ACC) and bivariate root mean square error (RMSE) are calculated using the
213 observed and hindcast RMM indices to represent the forecast skills of the IAP-CAS model as

$$214 \text{ACC}(\tau) = \frac{\sum_{t=1}^N [a_1(t)b_1(t,\tau) + a_2(t)b_2(t,\tau)]}{\sqrt{\sum_{t=1}^N [a_1^2(t) + a_2^2(t)]} \sqrt{\sum_{t=1}^N [b_1^2(t,\tau) + b_2^2(t,\tau)]}}, \text{ and} \quad (5)$$

$$215 \text{RMSE}(\tau) = \sqrt{\frac{1}{N} \sum_{t=1}^N [(a_1(t) - b_1(t,\tau))^2 + (a_2(t) - b_2(t,\tau))^2]} \quad (6)$$

216 Here $a_1(t)$ and $a_2(t)$ are the observation RMM1 and RMM2 at time t ; $b_1(t)$ and $b_2(t)$ are the forecasting RMM1 and
217 RMM2 at time t for lead τ days; N is the total number of times. It is commonly accepted that days with ACC above 0.5 are

218 considered to have valid forecasts. Therefore, the forecast skill of a model is quantitatively defined as the maximum lead time
 219 exceeding 0.5, which approximately corresponds to the day when RMSE reaches $\sqrt{2}$.

220 RMM index can also be adapted to quantitatively evaluate the forecasted intensity and velocity through the calculation of the
 221 error of amplitude ($ERR_{amp}(\tau)$) and phase ($ERR_{phase}(\tau)$) as a function of lead time τ :

$$222 \quad ERR_{amp}(\tau) = \frac{1}{N} \sum [AMP_b(t, \tau) - AMP_a(t)], \text{ and} \quad (7)$$

$$223 \quad ERR_{phase}(\tau) = \frac{1}{N} \sum \tan^{-1} \left[\frac{a_1(t)b_2(t, \tau) - a_2(t)b_1(t, \tau)}{a_1(t)b_1(t, \tau) + a_2(t)b_2(t, \tau)} \right] \quad (8)$$

224 Negative (positive) $ERR_{amp}(\tau)$ indicates weaker (stronger) amplitude in forecasts. Similarly, Negative (positive)
 225 $ERR_{phase}(\tau)$ indicates slower (faster) propagation in forecasts. Here the MJO amplitude for observation ($AMP_a(t)$) and
 226 forecast ($AMP_b(t, \tau)$) is defined as

$$227 \quad AMP_a(t) = \sqrt{a_1(t)^2 + a_2(t)^2}, \text{ and} \quad (9)$$

$$228 \quad AMP_b(t, \tau) = \sqrt{b_1(t, \tau)^2 + b_2(t, \tau)^2}. \quad (10)$$

229 3.3 Cluster analysis of MJO events

230 Another crucial method used in this research is the cluster analysis. In Section 5, we select the representative MJO events and
 231 classify them following the work Wang et al. (2019) did. This facilitates a more focused and targeted investigation into the
 232 forecast bias of MJO in the IAP-CAS model.

233 An MJO event was chosen if the regional average of OLR, spanning from 10° S to 10° N and 75° E to 95° E, remained below
 234 one standard deviation for a consecutive period of 5 days during the boreal winter (November–April). Subsequently, the K-
 235 means cluster analysis is employed to categorize the chosen MJO events based on the propagation patterns from day -10 to 20
 236 (day 0 is the day with the peak MJO in the Indian Ocean). At last, we use silhouette clustering evaluation (Rousseeuw, 1987)
 237 criteria to identify and eliminate poorly classified MJO events.

238 Finally, a total of 50 MJO events were selected from 1999 to 2018 winter and four types of MJO events were identified, namely
 239 the fast-propagating (10 cases), slow-propagating (16 cases), standing (12 cases), and jumping (12 cases) patterns of MJO (Fig.
 240 5).

241 The fast-propagating MJO and slow-propagating MJO belong to the propagating type of MJO, characterized by their
 242 consecutive eastward propagation across the Indian Ocean to the Pacific Ocean region. On the other hand, the standing and
 243 jumping MJO represent relatively non-propagating types, where the convection remains relatively fixed or exhibits
 244 discontinuous movement. Wang et al. (2019) believe that propagating MJO events are often associated with
 245 strong and tightly coupled Kelvin waves, especially for fast-propagating MJO. This is the biggest difference between
 246 propagating MJO and non-propagating MJO.

248 The evaluation in this section was conducted for the annual MJO events. Figure 3 demonstrates the overall MJO forecast skill
 249 in the IAP-CAS model and the improvement brought by the time-lagged ensemble method. Figure 3a shows the forecast skill
 250 of the ensemble mean is 24 days with the criterion of ACC exceeding 0.5, while the skill of individual members is about 21-
 251 22 days. Meanwhile, the ensemble mean RMSE reaches $\sqrt{2}$ at 21 days and the individual members exhibit larger RMSE,
 252 reaching $\sqrt{2}$ at 16 days (Fig. 3b). The solid blue line in Figure 3b represents the ensemble spread (Leutbecher and Palmer,
 253 2008) of IAP-CAS. When this ensemble spread approaches the RMSE of the ensemble mean (solid red line), it indicates that
 254 the ensemble members are sufficiently dispersive. Figure 3b illustrates that the ensemble exhibits an underdispersive
 255 characteristic in the early stage of the forecast. We have also observed similar issues of "underdispersive" in many other
 256 models (Rashid et al., 2011; Neena et al., 2014; Kim et al., 2014b; Xiang et al., 2015), and addressing this aspect may be a
 257 focal point for future model enhancements.

258 Increasing the number of ensemble members within a certain range proves effective in forecasting the uncertainty of weather
 259 and climate (Hou et al. 2001). We employed the time-lagged ensemble method to further augment the ensemble members. The
 260 time-lagged ensemble includes the ensemble members generated on the forecast day and from lag times. For instance, by
 261 incorporating ensemble members with a lag of i ($i = 0, 1, 2, \dots$) days, the total number of members becomes $4 * (i + 1)$.
 262 Upon examining the relationship between lag i days and forecast skill, it was found that the skill increases as i increases at
 263 first, but then it reaches a plateau when $i > 3$ (see Fig. A23). This suggests that the forecast skill of the 16 members may
 264 represent the limit of the time-lagged ensemble method in IAP-CAS. Figure 3d shows the ensemble of 16 members is more
 265 dispersive than 4 members, which is illustrated by less distinction between RMSE and Spread in the 16-member system. The
 266 ensemble mean of 16 members achieves a skill of 26 days, surpassing the skill of 4 members by two days (Fig. 3c).

267 Numerous prior investigations have demonstrated that MJO forecast skill is sensitive to the MJO amplitude in many models
 268 (Lin et al., 2008; Rashid et al., 2011; Wang et al., 2014; Xiang et al., 2022), and this characteristic is also evident in the IAP-
 269 CAS model. We classify an MJO case as an initial (target) strong case if its initial (target) amplitude is greater than 1, while
 270 an event with an initial (target) amplitude less than 1 is classified as an initial (target) weak case. Figures 4a-b show that in the
 271 IAP-CAS model, the forecast skills of strong MJO cases are generally higher than weak cases, especially in the target strong
 272 (weak) cases.

273 The amplitude and phase of MJO serve as additional indicators for a detailed assessment of MJO forecast performance. For
 274 initially strong MJO cases, we analyze the MJO amplitude and forecasted phase angle error (Figs. 4b-c). The individual
 275 member has a stronger amplitude than observation, which leads to a relatively strong amplitude in the ensemble mean during
 276 the initial 40 days. However, as the noise rapidly increases, the phase error of the individual members also escalates (as shown
 277 in Fig. 4c). The phase error results in a mutual cancellation in positive and negative phases of MJO among ensemble members,

278 leading to a rapid weakening of the amplitude in the ensemble mean. In Figure 4d, the phase error of the ensemble mean
279 indicates that the speed of forecasted MJO tends to decrease at first and then start increasing around the 10th day. A more
280 detailed investigation into the speed of propagating MJO events will be described in Section 5.

281 **5 The forecast of MJO propagation**

282 We present a qualitative diagnostic of a 20-year hindcast experiment to evaluate the overall forecast skills of IAP-CAS in
283 Section 4. This analysis provides us with preliminary insights into the performance and biases of the system. Given that the
284 MJO is more pronounced during boreal winter, our focus is concentrated from November to the following April. Based on
285 Wang et al. (2019), we aim to conduct further investigations into different types of boreal winter MJO events to explore the
286 physical explanation of system biases.

287 In Section 3, we have already described the methodology for classifying MJO events and results. Figure 5 compares the
288 composited propagation patterns of precipitation and U850 between observation and forecast for four different MJO types. In
289 observations, the fast-propagating (Fig. 5a) and slow-propagating (Fig. 5b) MJO exhibit a consecutive eastward propagation
290 structure from the Indian Ocean across the MC region to the Pacific Ocean. The primary distinction between the two types lies
291 in their propagation speed. The fast-propagating MJO demonstrates a faster speed, with a velocity of 4.58 m/s, compared to
292 the slow-propagating type, which moves at 4 m/s.~~The basic distinction between the two types is that the first type of MJO~~
293 ~~exhibits a faster propagation speed compared to the second type.~~ The standing MJO (Fig. 5c) remains relatively stationary
294 over the Indian Ocean and does not continue to propagate eastward. The jumping MJO (Fig. 5d) shows a convective system
295 that bypasses the MC region and directly jumps from the Indian Ocean to the Pacific Ocean. Here, fast MJO and slow MJO
296 are considered propagating MJO events, while the latter two types are regarded as non-propagating MJO events.

297 The observed U850 displays a coupled structure characterized by equatorial westerly anomalies of the Kelvin wave component
298 located west of the convection, and easterly anomalies of the Rossby wave component located east of the convection (Rui and
299 Wang, 1990b; Adames and Wallace, 2014; Wang and Lee, 2017). As illustrated in Figure 5, a distinct contrast between
300 propagating MJO and non-propagating MJO can be found in the circulation at the low level: in the propagating MJO events,
301 the Kelvin wave response is strong and tightly coupled with the center of convection, which is shown in the stronger and
302 eastward-extending easterly wind component, particularly prominent in fast MJO events. Many previous studies (Benedict
303 and Randall, 2007; Hsu and Li, 2012; Wang and Lee, 2017) have also indicated that the presence of low-level easterly winds
304 is a key signal that contributes to the eastward propagation of MJO by inducing low-level convergence and premoistening to
305 the east of the major convection. In the non-propagating MJO events, the easterly wind is weak and tends to decouple from
306 the major convection.

307 From the Hovmöller diagram of observed propagating MJO (Fig. 5), a significant change in convection is observed after
308 crossing the MC region, which is marked by a decrease in intensity and a slower propagation speed. This change is roughly
309 delineated by the 135° E, which is commonly referred to as the “MC barrier”. As mentioned above, the “MC barrier” effect is
310 usually amplified in the climate models. This phenomenon is also observed in the forecast of slow MJO events in the IAP-
311 CAS model. The forecasted convective signal of slow MJO gradually fades after crossing the MC. However, in the forecast of
312 fast MJO, the convection does not exhibit a significant decrease in intensity after crossing the MC region, and the speed of the
313 propagation appears to be relatively faster compared to observations in both fast and slow MJO events. The model accurately
314 reproduces the propagating morphology of the MJO and exhibits coupled signals of Kelvin and Rossby waves (Figs 5e and
315 5f). However, a noticeable acceleration in speed is evident, particularly in the case of fast MJO, reaching speeds of 6 m/s,
316 while the simulated slow MJO moves at 5 m/s. Figure 5g also shows that the forecast for standing MJO remains somewhat
317 imprecise. The forecasted convection is weak, and there are signals in both the Indian Ocean and the Pacific Ocean, whereas
318 observed standing MJO only indicates strong convective signals in the Indian Ocean. This aspect is also evident in the MJO
319 forecast skill depicted in Figure A46, where the standing MJO has the lowest skill (13 days). For each MJO type, we consider
320 the skill as the ACC of the cases initiated from day -20 to day 15 (Xiang et al., 2015). Figure A4-6 displays that the fast MJO
321 achieves the highest skill at 32 days, while the jumping MJO and slow MJO exhibit skills of 23 and 21 days, respectively.

322 Additionally, from the Hovmöller diagram of observed propagating MJO (Figs. 5a and 5b), a significant change in convection
323 is observed after crossing the MC region, which is marked by a decrease in intensity and a slower propagation speed. This
324 change is roughly delineated by the 135° E, which is commonly referred to as the “MC barrier”. As mentioned above, the “MC
325 barrier” effect is usually amplified in the climate models. In the IAP-CAS model, the forecasted convective signal of slow
326 MJO appears to halt after crossing the MC region. Could this indicate an amplification of the "MC barrier" issue in the IAP-
327 CAS model? However, this phenomenon is less pronounced in the simulation of fast MJO. Due to the zonal averaging in the
328 Hovmöller diagram, some information may be obscured. Further investigation is required to determine the detailed
329 characteristics of the propagating MJO simulated by the model.

330 In this work, we focus specifically on the analysis of propagating MJO events which have relatively complete propagation
331 processes. Figures 6 and 7 presents the evolution patterns of propagating MJO. In the first 10 days, it is noticeable that the
332 forecasted precipitation intensity of propagating MJO is significantly higher than observed, especially in the case of fast MJO.
333 Coupled winds in 850 hPa also exhibit stronger magnitudes, with a larger zonal scale. It is noticeable in both the spatial
334 propagation diagram (Fig. 6) and the phase diagram (Fig. 7) that the forecasted precipitation intensity is significantly higher
335 than the observed, indicating the presence of a stronger convective system of forecasted fast MJO. The forecasted location of
336 the major convection is relatively biased towards the east (Fig. 6b), which further confirms that means there is an overestimation
337 of the propagation speed. The phase diagram also indicates a higher speed, with the blue points propagating faster than the red
338 points (Fig. 7a). On the 15th day, the MJO convective system crosses the MC region and reaches the eastern Pacific (Figs. 6a-

b). It is worth noting that the forecasted negative phase of MJO exhibits a significant development, with an accelerated speed, gradually intruding into the positive phase (Figs. 7b and 7d). By the 20th day, the development of the negative phase has further intensified, extending its influence into the tropical eastern Pacific region, while in the observation, the negative phase remains east of the MC region. ~~A similar phenomenon is also evident in the forecasts of slow MJO events. Figures 6c-d and 7b show that the amplitude of slow MJO is weaker than fast MJO. There are still biases of stronger convection and faster propagation in the forecast of slow MJO.~~ In the later stages, as the negative phase intrudes, the forecasted convective signal in the positive phase is almost absent due to the inherently weaker convection in slow MJO. ~~This amplification of the “MC barrier” in the forecast of slow MJO may contribute to the diminished convective signal. The intrusion of negative phase convection is also observed in forecasted fast MJO. However, due to the relatively strong positive phase convection in the forecast of fast MJO, it is less evident in the zonal mean, as shown in the Hovmöller diagram. The disappearance of the slow MJO signal observed in the Hovmöller diagram after crossing the MC region may stem from the intrusion of the negative phase. This might differ from the commonly defined issue of “MC barrier” amplification observed in many models.~~ ~~In Figure A3, simulations show that both standing and Jumping MJO also exhibit overall enhanced convective intensity. However, they accurately capture the non-propagating characteristics of the observed MJO, such as the weak coupling of Kelvin waves and the strong coupling of Rossby waves.~~

6 The possible physical explanation for the forecast biases

Section 5 highlights some biases observed in the forecast of propagating MJO, which includes stronger amplitude and faster propagation speed in the IAP-CAS model. These biases are also mentioned in Section 4. In this section, we aim to unravel the physical mechanisms underlying these biases.

As a large-scale convective system, MJO’s genesis, evolution, and dissipation are intricately linked to atmospheric moisture (Wang, 1988; Kemball-Cook and Weare, 2001; Maloney, 2002; Wang and Lee, 2017). Given that the model forecasts exhibit a systematic bias of stronger amplitude, we start with the diagnosis of the background state in moisture. Figure 8 shows the winter mean specific humidity averaged over 10° S–10° N. A clear positive bias of the background moisture state in the IAP-CAS model is observed (Fig. 8c), which can enhance the convection in the MJO. However, the distribution of this moisture bias is non-uniform. Figure 8c illustrates that the positive moisture bias is more pronounced towards the western Indian Ocean and the central-eastern Pacific, and this bias gradually spreads to the upper levels. However, in the MC region, the positive moisture bias is smaller and primarily concentrated in the low level. We speculate that higher evaporation fluxes in the model may be the reason for the positive moisture bias. ~~Furthermore~~ ~~Therefore~~, the reduction in oceanic surface area within the MC region contributes to a decrease in this positive bias.

368 Figure 9 displays the precipitation-induced condensational heating (Q_2) during fast MJO and slow MJO events. The
369 condensational heating serves as a proxy for the distribution of convection, which was estimated by the moisture sink defined
370 as

$$371 \quad Q_2 = -L_v \left(\frac{\partial q}{\partial t} + \vec{V} \cdot \nabla q + \omega \frac{\partial q}{\partial p} \right), \quad (11)$$

372 where q is the specific humidity, \vec{V} is the horizontal circulation, ω is vertical pressure velocity, and L_v is the latent heat
373 at condensation, which is a constant here. The vertical distribution of Q_2 reveals that both fast MJO and slow MJO events in
374 the model forecasts trigger stronger convection, particularly in the fast MJO events. Furthermore, the enhanced convective
375 heating leads to a strong response in the coupled MJO-related circulation (Fig. 9). ~~On the 10th day, both the fast MJO and the~~
376 ~~slow MJO experience further intensification in the model. This intensification can be attributed to the amplification of the~~
377 ~~positive moisture bias following the departure from the MC region. From the 1st day to the 10th day, there is a gradual~~
378 ~~strengthening process observed in the simulated convection, particularly pronounced in fast MJO, with its intensity peaking~~
379 ~~on the tenth day.~~

380 To further understand the ~~faster propagation and intensity variations~~ of MJO in the IAP-CAS model, it is necessary to
381 comprehend the underlying physical processes associated with ~~the propagation of MJOit~~. Under the framework of “moisture
382 mode”, Jiang (2017) performed a moisture budget analysis on the latest generation of general circulation models (GCMs) and
383 identified the key processes for the eastward propagation of MJO. This research revealed that the advection ($\vec{V} \cdot \nabla \bar{Q}$) of the
384 seasonal mean moisture (\bar{Q}) by the MJO anomalous circulations (\vec{V}) plays a crucial role in the propagation of MJO. By
385 increasing moisture eastward and decreasing it westward of the MJO convection, the advection regulates the propagation.
386 (Kim et al., 2014a; Adames and Kim, 2016; Jiang et al., 2018). Among the two determining factors (\vec{V} and \bar{Q}), the role of the
387 moisture gradient term is further emphasized. Many studies (Gonzalez and Jiang, 2017; DeMott et al., 2018; Ahn et al., 2020)
388 have demonstrated that the mean moisture's horizontal gradient plays a crucial role in determining the propagation of MJO
389 (Fig. 10a). It is well-forecasted in the models that simulate MJO well, leading to realistic horizontal mean moisture gradients
390 and, thus, well-forecasted horizontal moisture advection associated with the MJO (Hsu and Li, 2012; Kim et al., 2014a; Nasuno
391 et al., 2015; Adames and Wallace, 2015; Gonzalez and Jiang, 2017). The IAP-CAS model is capable of reproducing this
392 gradient, although there is an overall stronger moisture bias (Fig. 10b). Here, the \bar{Q} presented is the winter mean specific
393 humidity at 850 hPa (\bar{Q}_{850}). Research has indicated that the \bar{Q}_{850} is representative (Kim, 2019), and subsequent analysis also
394 focuses on the 850 hPa level.

395 Figure 11 shows the composite equatorial U850 ~~anomalies~~ averaged over the 15° S-15° N for fast MJO and slow MJO
396 respectively. It depicts the transition from westerly to easterly winds in the MC region (as enclosed by the two blue dashed
397 lines), leading to the change from positive advection to negative advection. On the 1st and 5th days, the MC region is
398 predominantly occupied by easterly winds, while from the 10th to the 20th day, the region is primarily characterized by westerly

399 winds in both fast MJO and slow MJO. However, the forecasted amplitude of low-level wind is significantly stronger, which
400 can be caused by the enhanced MJO convection as explained earlier.

401 The MJO anomalous circulation patterns in the MC region result in a positive moisture advection on the eastern part of the
402 MJO during the early stages of MJO's development, which facilitates the propagation of convection in the positive phase. We
403 refer to this process as the "developing phase". Figure 12 provides a detailed illustration of this process. Conversely, during
404 the later stages, there is a negative moisture advection on the western side of the MJO, which leads to the propagation of
405 convection in the negative phase and promotes the dissipation of the MJO. We refer to this process as the "decaying phase"

406 (Fig. 12). Compared to the observation, the stronger amplitude of the low-level moisture advection ($\overline{\vec{V}'} \cdot \nabla \overline{Q}$) in the model
407 explains the gradual enhancement of convective moist phases during the early stages and the amplification of convective dry
408 phases during the later stages ~~accelerated positive phase of convection during the early stages and the accelerated negative~~
409 ~~phase during the later stages~~ (Fig. 13). ~~This explains the increasing propagation speed of the forecasted MJO. In the observation,~~
410 ~~the amplitude of the moisture advection during fast MJO events is stronger than that during slow MJO events, further~~
411 ~~confirming this physical explanation. The model's moist environment leads to intensified convection, triggering the~~
412 ~~strengthening of coupled winds, which in turn enhances the moist phase in the early stage and the dry phase in the later stage~~
413 ~~of convection. Consequently, during the development phase of the MJO, its amplitude gradually strengthens. Conversely,~~
414 ~~during the decaying phase of the MJO, the intensity of the dry phase also progressively increases.~~

415 As the simulated propagating MJO gradually intensifies, we observe an enhancement of easterly winds on the east of the
416 convective center, accompanied by an overestimation in zonal scale, indicating the triggering of stronger Kelvin waves (Figs
417 7b and 7d). According to Wang et al. (2019), MJO with a larger zonal scale will experience an increased eastward propagation
418 speed since the phase speed is inversely proportional to the wave number. This phenomenon is also observed in observation,
419 where the Kelvin wave response to fast MJO exhibits a larger zonal scale compared to slow MJO. Subsequently, during the
420 decay phase of the propagating MJO, the model exhibits a pronounced Rossby wave response triggered by the MJO, leading
421 to the intrusion of convective negative phases and facilitating the dissipation of the MJO.

422 In addition to examine the winter mean moisture state (\overline{Q}), we have analyzed MJO-related moisture anomalies (Q') as well
423 (Fig. 14). By comparing the evolution pattern of moisture anomalies between slow MJO and fast MJO, it is found that the
424 moisture anomalies in the eastern part of fast MJO are more intense compared to the slow MJO. This results in stronger low-
425 level moisture transport towards the convective region, thereby also facilitating the intensification and acceleration of the MJO.
426 Moreover, there is a significant distinction in the spatial correlation between fast and slow MJO and it happens as early as the
427 1st day. As the forecast lead time progresses, the accuracy of the moisture forecast deteriorates, while fast MJO events display
428 comparatively better performance. The disparity in moisture anomalies is possibly a pivotal factor contributing to differences
429 in forecast skills between the fast (32 days) and the slow MJO (21 days). This underscores the significance of improving
430 moisture forecast in the MJO forecast.

431 7 Summary and discussion

432 7.1 Summary

433 The graphical abstract presents a workflow for this paper, outlining the structure of this work. This study introduces a newly
434 developed S2S ensemble forecast system of the IAP-CAS model. The introduction primarily focuses on the numerical model,
435 initialization, ensemble generation, and post-processing aspects of the S2S system. Then we aim to identify potential
436 possibilities for developing this S2S system through a comprehensive assessment of its forecast skills. Based on the 20-year
437 hindcast experiment, the IAP-CAS model shows comparable skill (24 days) to other S2S models. However, the ensemble
438 forecast for MJO has been demonstrated to be underdispersive. A detailed examination of the propagating MJO forecasted in
439 the IAP-CAS model reveals that the amplitude of the convection is overestimated with an increasing propagation speed,
440 particularly in the fast MJO events. These biases are accompanied by a faster dissipation of the MJO.

441 The root cause of these biases lies in the model's wetter environment, which leads to enhanced convection and strengthened
442 circulation coupled with convection, ~~and subsequently, stronger moisture convection.~~ This, in turn, further amplifies
443 convection during the development of propagating MJO. The gradual intensification of MJO strength and coupled Kelvin
444 waves increasing propagation speed in the MJO propagation is mainly associated with the stronger amplitude of the low-level
445 moisture advection ($\vec{V}' \cdot \nabla \bar{Q}$) in the forecast. The overestimate in the zonal scale of Kelvin waves accelerates the propagation
446 of the propagating MJO in the model. Similarly, the strengthening of Rossby waves also hastens the dissipation of the MJO.
447 Moreover, the differences in forecast skills between the fast MJO and the slow MJO may be attributed to discrepancies in
448 moisture anomalies (Q') forecast. This further underscores the significance of accurate moisture forecasts.

449 7.2 Discussion

450 In Figures A5A4, we compare the forecast skill of the IAP-CAS model with ~~ten~~ 11 other S2S models. The MJO index of ~~11~~
451 12 S2S models and ERA-Interim from the S2S website (<http://www.s2sprediction.net/>) is used for evaluation during the
452 standard hindcast period ~~1999~~ 2001-2010. In Figure A4, we observe improved forecast skill in ensemble forecasts compared
453 to deterministic forecasts. Among the ~~11~~ 12 S2S models, the IAP-CAS model exhibits MJO skill above the mean skill level,
454 while the ECMWF model stands out as the highest-performing model. Figure ~~A5b~~ A5a shows that the skill of individual
455 members in ECMWF is approximately 17-18 days, whereas the ensemble mean demonstrates an extended skill of up to 30
456 days. This phenomenon may be attributed to the ECMWF model's considerable dispersion (Fig. ~~A5C~~ A5b), which once again
457 underscores the critical role of ensemble dispersion in forecasting uncertainties of weather and climate.

458 Therefore, the forthcoming phase in our model's development plan encompasses increasing model dispersion through
459 improved ensemble perturbation methods, with the ultimate goal of improving model forecast skills. The method of orthogonal
460 conditional nonlinear optimal perturbations (CNOPs, Mu et al. 2003) and the second-order exact sampling (Pham, 2001) are
461 both promising approaches for generating initial perturbations in the model. This method allows the generation of a set of

462 initial perturbations in different orthogonal perturbation subspaces, each with the maximum potential for nonlinear
463 development. When applied to ensemble forecast using a simple Lorenz-96 model, the CNOPs method has demonstrated
464 higher forecast skill compared to the commonly used linear Singular Vectors (SVs) method (Lorenz, 1996). Furthermore,
465 PDAF (Parallel Data Assimilation Framework, Nerger et al., 2020) provides an efficient method known as second-order exact
466 sampling, which uses the long-time variability of the model dynamics to estimate the uncertainty. Evidence has already
467 suggested that the use of second-order exact sampling can greatly improve the skill in sea ice extent throughout the Arctic and
468 along the Northern Sea Route (Yang et al., 2020). We plan to explore the application of CNOPs and second-order exact
469 sampling in the IAP-CAS model in the future and eagerly anticipate the potentially significant results it may yield. Additionally,
470 using machine learning to improve the skill of ensemble forecast is also a viable way to enhance the ensemble forecast of our
471 model.

472 In addition to exploring ensemble perturbations, we also intend to enhance the initialization system of the model. Recognizing
473 the moisture is crucial in the forecast of MJO and acknowledging the issue of moisture bias in the IAP-CAS model, it is
474 essential to take measures to ameliorate moisture forecast in our model. The recent research by Zeng (Zeng et al., 2023)
475 provides convincing evidence that humidity initialization can indeed significantly enhance MJO forecast in the IAP-CAS S2S
476 forecast system, especially in the 2 and 3 phase of MJO propagation. However, it is worth noting that changes in the mean
477 state have a significant impact on MJO development (Hannah et al., 2015; Kim, 2019), we must pay attention to the influence
478 of moisture initialization on the mean state. Moreover, the current S2S system's initialization process uses the nudging method,
479 and it is worthwhile to explore more efficient methods to enhance the initialization process.

480 We are also considering increasing the resolution of the model to C384 (25 km) globally. A High-resolution coupled model
481 could better represent the MJO (Crueger et al., 2013). This improvement could be attributed to the enhanced resolution, which
482 better captures the ocean-atmosphere interaction – a critical factor for MJO convection. Increasing the resolution is also
483 meaningful for enhancing forecasts in the MC₂ region by accurately depicting terrain distortion (Hsu and Lee, 2005; Inness and
484 Slingo, 2006; Wu and Hsu, 2009). Further optimizing the model's physical processes and dynamic-physical coupling is also
485 believed to enhance the forecast of the MJO (Zhou and Harris, 2022). As the foreseeable resolution and complexity of the
486 model increase in the future, the issue of power consumption on X86 architecture processors for handling the growing amount
487 of data will become more pronounced. We have plans to port the model to the computing platform based on ARM architecture
488 to address the challenges posed by the explosive growth of data.

Component	Model name	Horizontal Resolution	Vertical levels	Reference
Atmosphere	FAMIL2	Cubed Sphere Grid (C96, ~1°×1°)	32 in the hybrid levels	Li et al. 2019
Land	CLM4.0	Nested subgrid hierarchy (f09, ~1°×1°)	15 soil levels and 3 snow levels	Oleson et al. 2010; Lawrence et al. 2011
Ocean	POP2	Displaced-pole grid (gx1v6, ~1°×1°)	60 levels	Kerbyson and Jones 2005
Sea ice	CICE4	Displaced-pole grid (gx1v6, ~1°×1°)	5 levels	Hunke et al. 2010

~~Table 2 Hybrid coefficient of hybrid sigma-pressure coordinates at layer interfaces in CAS EGOALS-f2~~

Layer	Coefficient of pressure coordinates	The coefficient of sigma coordinates	Layer	Coefficient of pressure coordinates	The coefficient of sigma coordinates
1	100.00	0.00	18	27131.33	0.23
2	400.00	0.00	19	24406.11	0.32
3	818.60	0.00	20	21326.05	0.42
4	1378.89	0.00	21	18221.18	0.51
5	2091.80	0.00	22	15275.15	0.59
6	2983.64	0.00	23	12581.68	0.67
7	4121.79	0.00	24	10181.43	0.73
8	5579.22	0.00	25	8081.90	0.79
9	7419.79	0.00	26	6270.87	0.83
10	9704.83	0.00	27	4725.35	0.87
11	12496.34	0.00	28	3417.39	0.91
12	15855.26	0.00	29	2317.75	0.93
13	19839.62	0.00	30	1398.09	0.96
14	24502.73	0.00	31	632.50	0.98
15	28177.10	0.02	32	0.00	0.99
16	29525.28	0.06	33	0.00	1.00
17	29016.34	0.14			

491 **Table 3 Initialization information of the S2S ensemble forecast system**

Nudging type	Data Assimilation	Variable	Data	Frequency
Reanalysis nudging	Time-Lagged Nudging (Hoffman and Kalnay, 1983; Jeuken et al., 1996)	U, V, T, P _s , z _s ^a SST	FNL (http://rda.ucar.edu/datasets/ds083.2 , ds083.2 DOI: 10.5065/D6M043C6) NOAA OISST (Reynolds et al., 2007)	6h
Forecast nudging		U, V, T, P _s , z _s	GFS weather forecast	6h

492 ^aTable notes: U represents zonal wind, V represents meridional wind, T represents temperature, P_s represents surface pressure,
 493 z_s represents surface geopotential height, and SST represents sea surface temperature.

Table 4 Introduction to the output data of the S2S ensemble forecast system

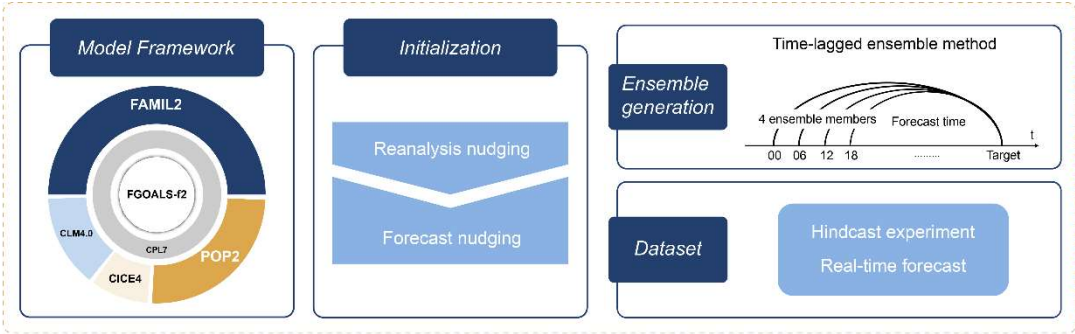
Experiment	Ensemble members	Time range	Frequency	Forecast time	Variable	Resolution	Interpolation method
Hindeast	4	1999-2018	Daily	65 days	25 variables	Horizontal: 1.5°	One-order
Real-time forecast	16	2019			(A detailed list of variables is shown in Table 5)	Horizontal: 1.5° Vertical: 7 levels (1000, 925, 850, 700, 500, 300, and 200hPa)	conservation

Statistical process	Level(s)	Short name	Standard name	Unit
Instantaneous value/24h	The variables are located on 10 pressure layers (1000, 925, 850, 700, 500, 300, 200, 100, 50, 10 hPa)	gh	Geopotential height	gpm
		t	Temperature	K
		u	U-velocity	m·s ⁻¹
		v	V-velocity	m·s ⁻¹
		w	Vertical velocity	pa·s ⁻¹
2-dimensional variables	The variable is located on 7 pressure layers (1000, 925, 850, 700, 500, 300, 200 hPa)	q	Specific humidity	kg·kg ⁻¹
		w	Vertical velocity	pa·s ⁻¹
		sp	Surface pressure	Pa
		ism	Land-sea mask	Proportion of land
Daily average value		orog	Orography	gpm
		tee	Total cloud cover	%
		skt	Skin temperature	K
		2t	Surface air temperature	K
		2d	Surface air dewpoint temperature	2d
		wtmp	Sea surface temperature	K
ei	Sea ice cover	proportion		

24-hour=	sf	Snow fall water equivalent	kg m⁻²
accumulated=	ttr	Time-integrated top net thermal radiation	W m⁻²s
value	ssr	Time-integrated surface net solar radiation	W m⁻²s
	str	Time-integrated surface net thermal radiation	W m⁻²s
	ssrd	Time-integrated surface solar radiation downwards	W m⁻²s
	strd	Time-integrated surface thermal radiation downwards	W m⁻²s
Instantaneous=	mx2t6	Surface air maximum temperature	K
value/6h	mn2t6	Surface air minimum temperature	K
	10u	10 metre u-velocity	m s⁻¹
	10v	10 metre v-velocity	m s⁻¹
6-hour=	tp	Total precipitation	kg m⁻²
accumulated=			
value			

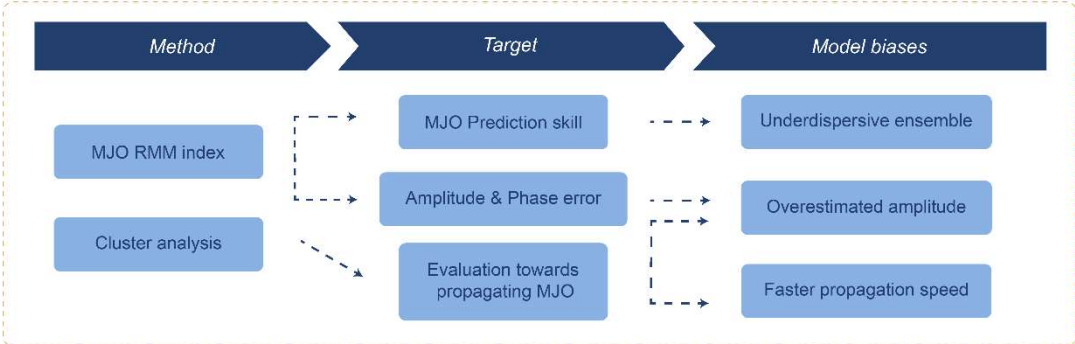
1 An overview of IAP-CAS S2S ensemble forecast system

EXPECTED: Readers can acquire a thorough and organized comprehension of this system



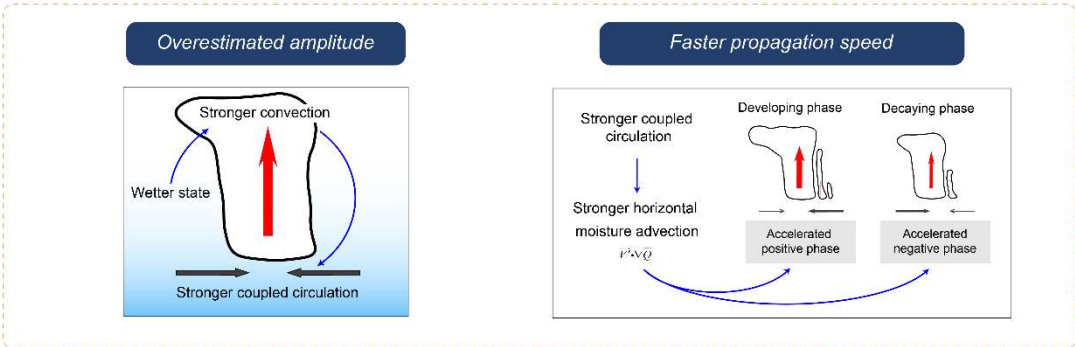
2 Evaluation of MJO forecast in IAP-CAS S2S system

EXPECTED: Gain insights into the S2S system's performance in S2S forecast



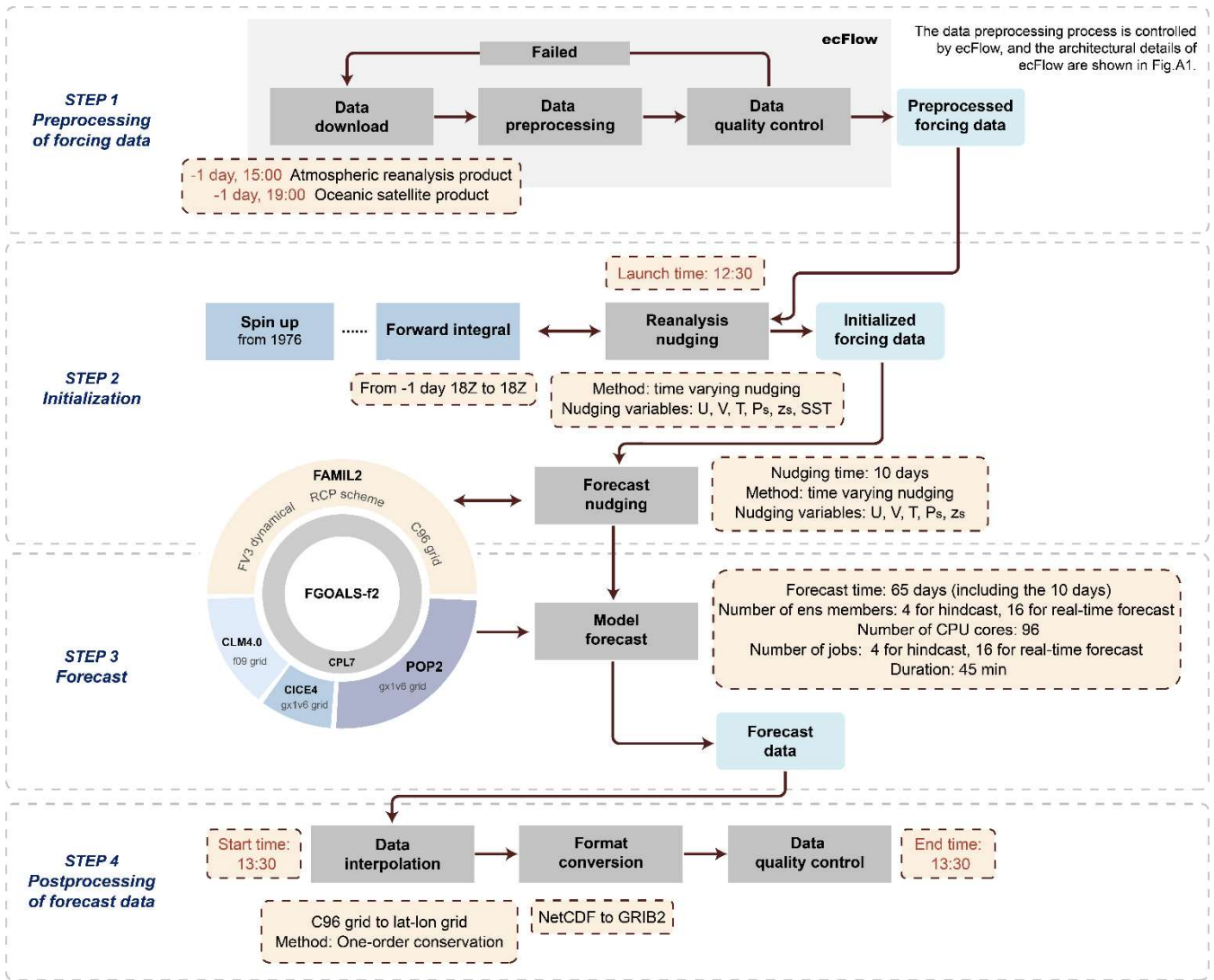
3 The possible explanation about the prediction biases

EXPECTED: Identify the sources of system errors for further improvements



496

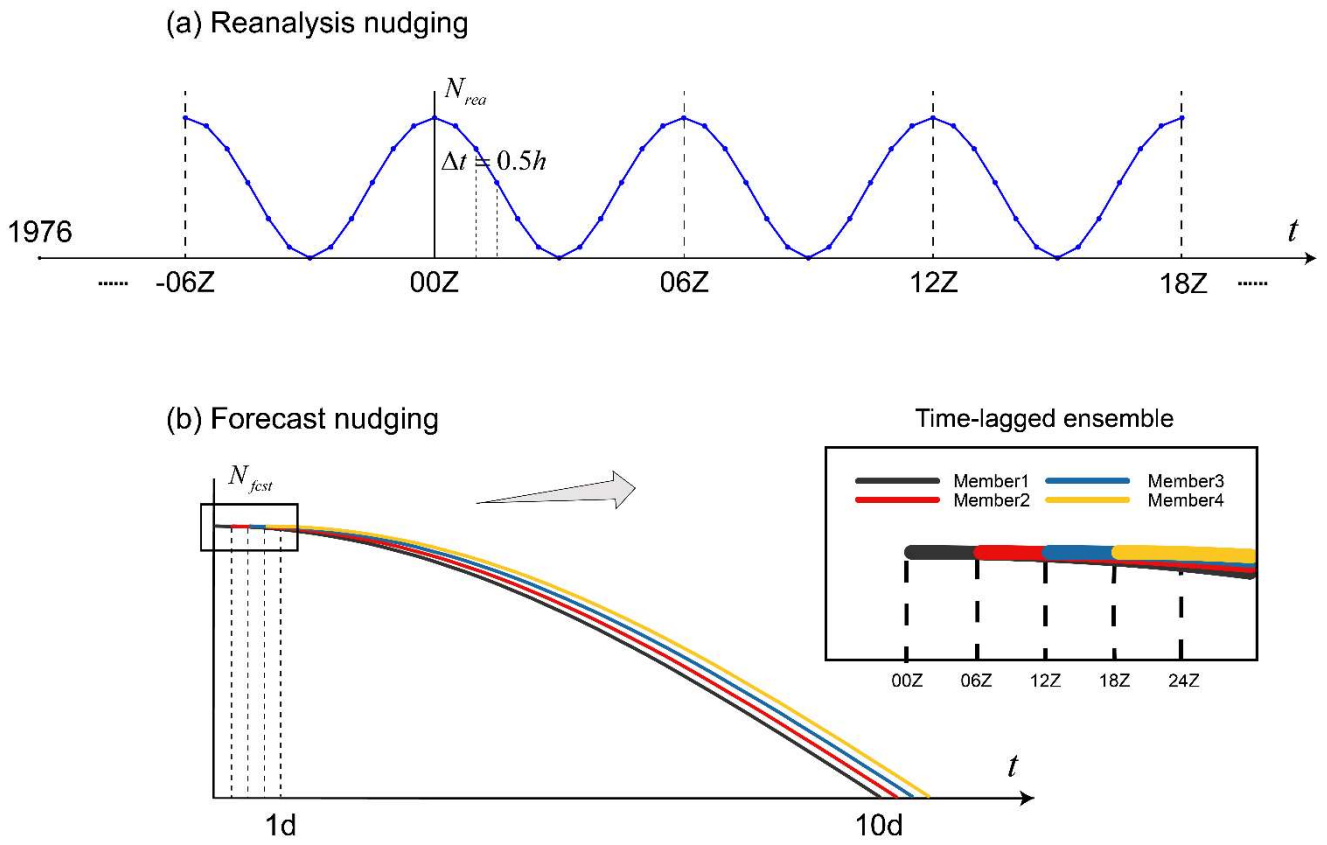
497 **The graphical abstract**



498
499

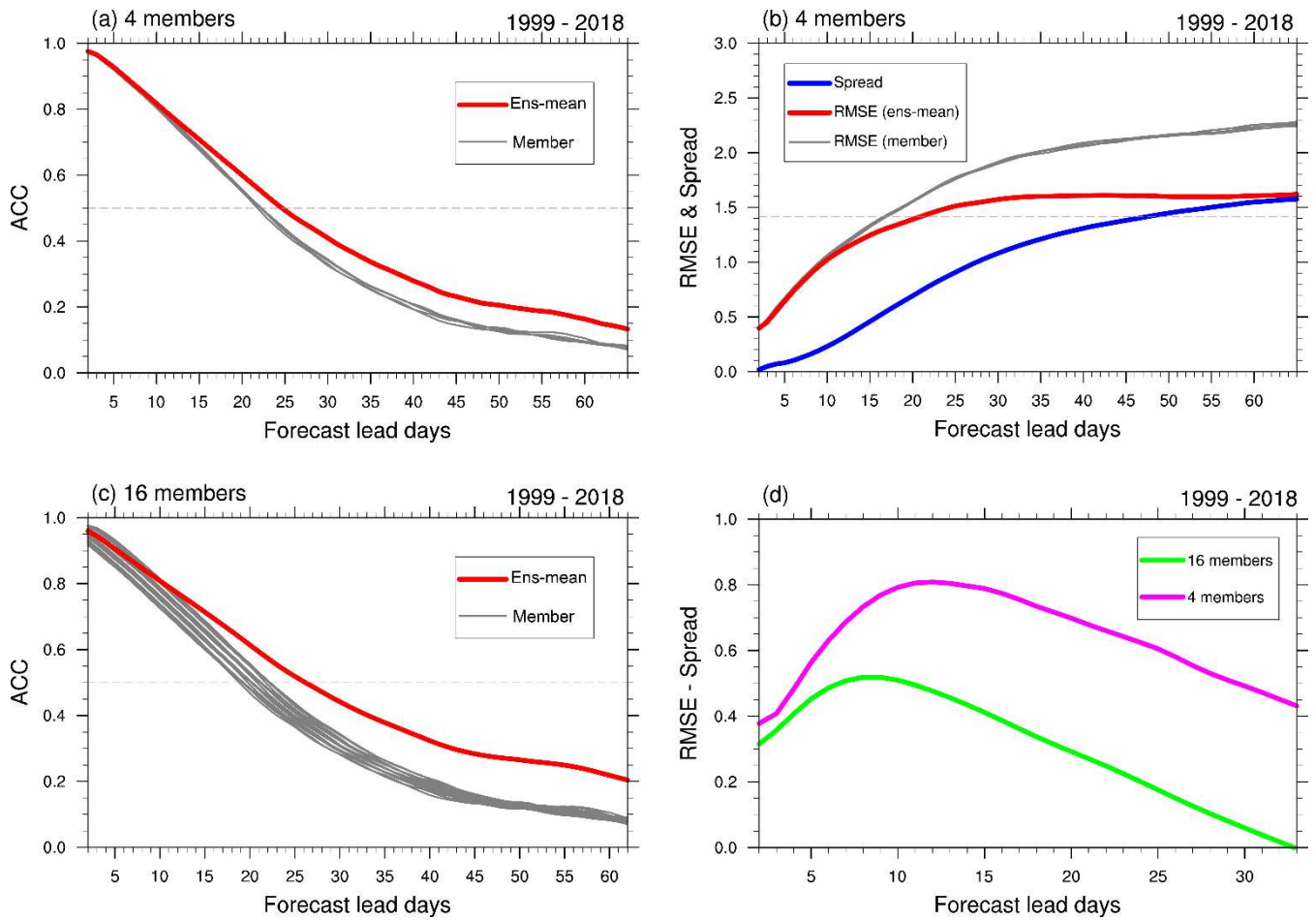
The time marked in red here is local time (beijing time)

Figure 1. The structure of the IAP-CAS S2S ensemble forecast system



500

501 **Figure 2. The initialization scheme of the S2S ensemble forecast system in the IAP-CAS model. The relaxation coefficient (N) as a**
 502 **function of time (t) in (a) the reanalysis nudging and (b) the forecast nudging. In (a), The reanalysis nudging begins on January 1,**
 503 **1976. The dots indicate the nudging process every 30 minutes. In (b), the solid lines of 4 colors represent the 4 ensemble members**
 504 **with their generation facilitated through the application of the time-lagged method.**



505

506

507

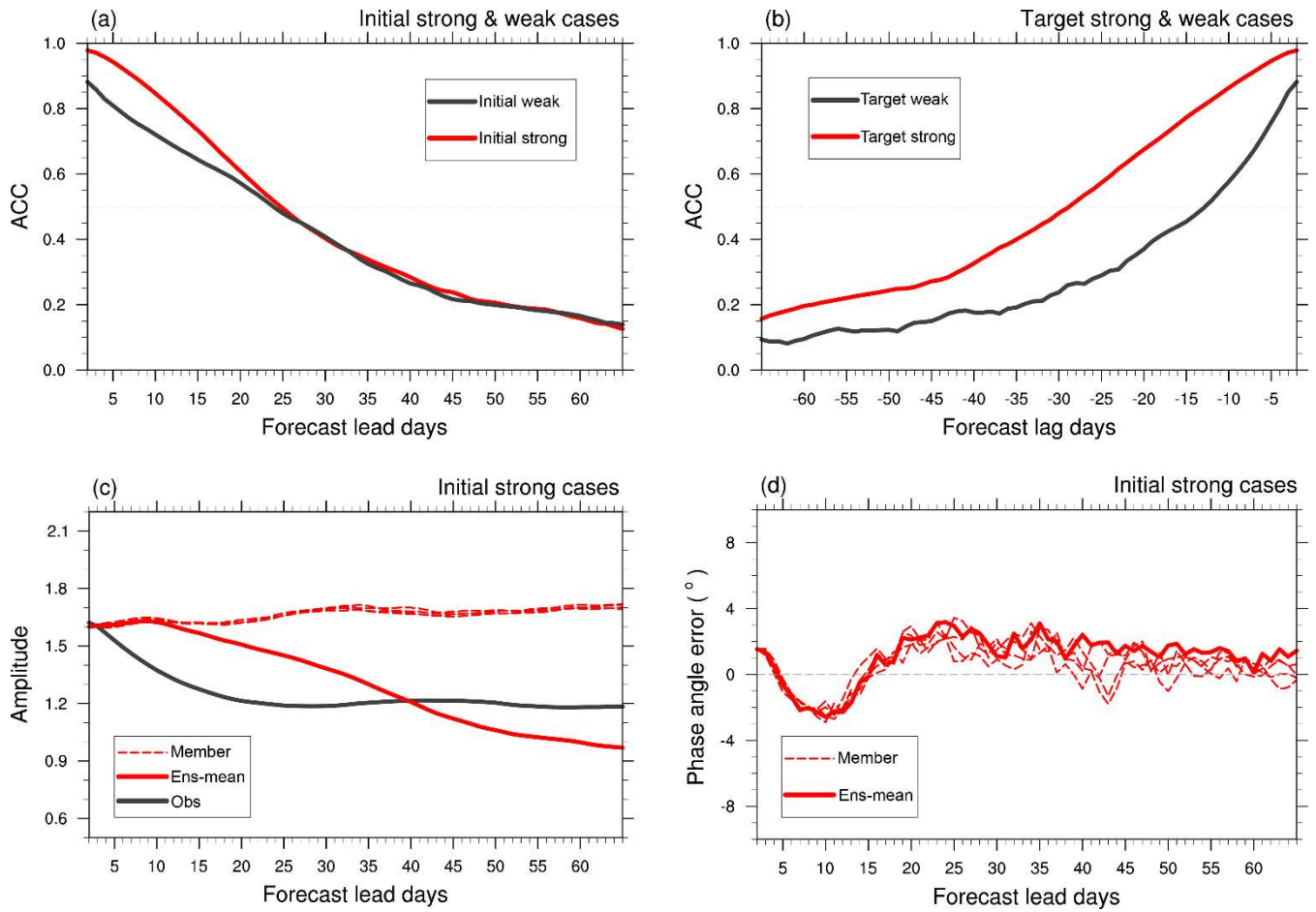
508

509

510

511

Figure 3. MJO forecast skill of IAP-CAS for the annual MJO events over 20 years (1999-2018) re-forecast data. (a) The bivariate anomalous correlation coefficient (ACC) and (b) The Root Mean Squared Error (RMSE) varied with forecast lead days for individual members (gray solid line) and ensemble mean (red solid line). The blue solid line denotes the ensemble spread. (c) The ACC of individual members and ensemble mean, as generated by the time-lag method resulting in 16 ensemble members. The dashed line in (a) and (c) has the values of 0.5, and it represents 1.414 in (b). (d) The difference between RMSE and Spread of 4-member ensemble mean (purple solid line) and 16-member ensemble mean (green solid line).



512

513

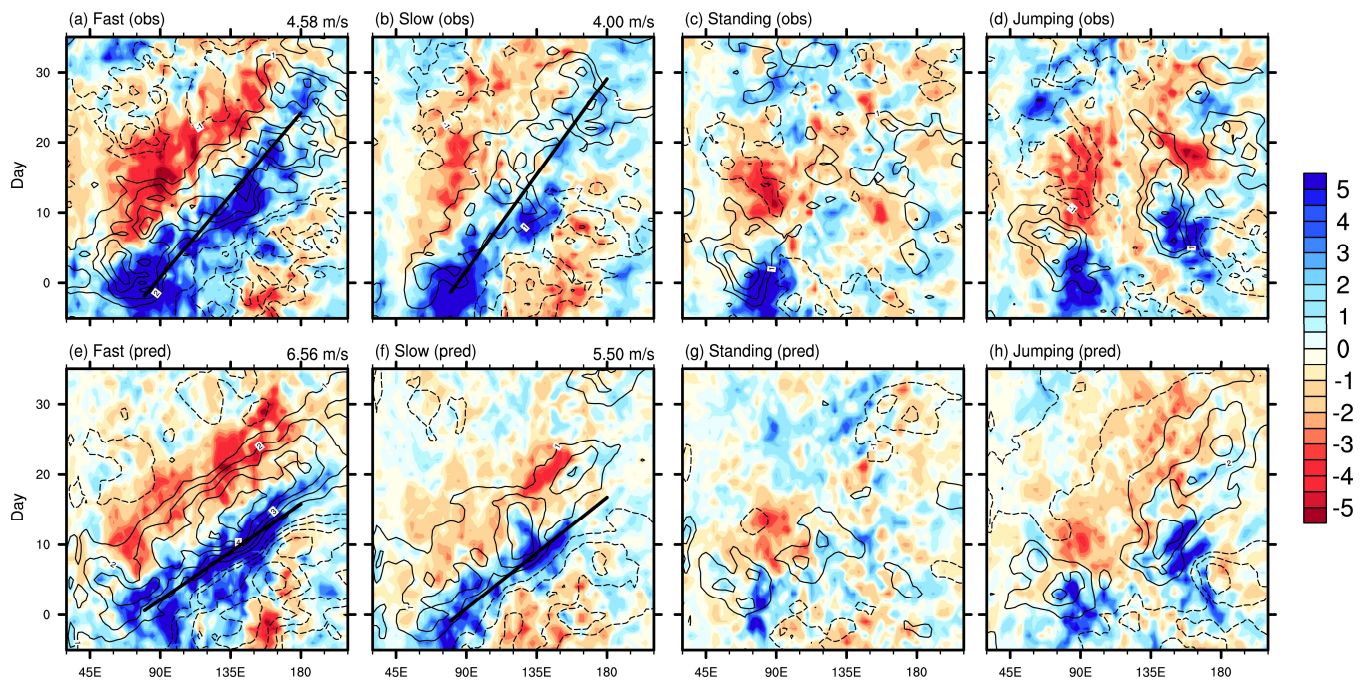
514

515

516

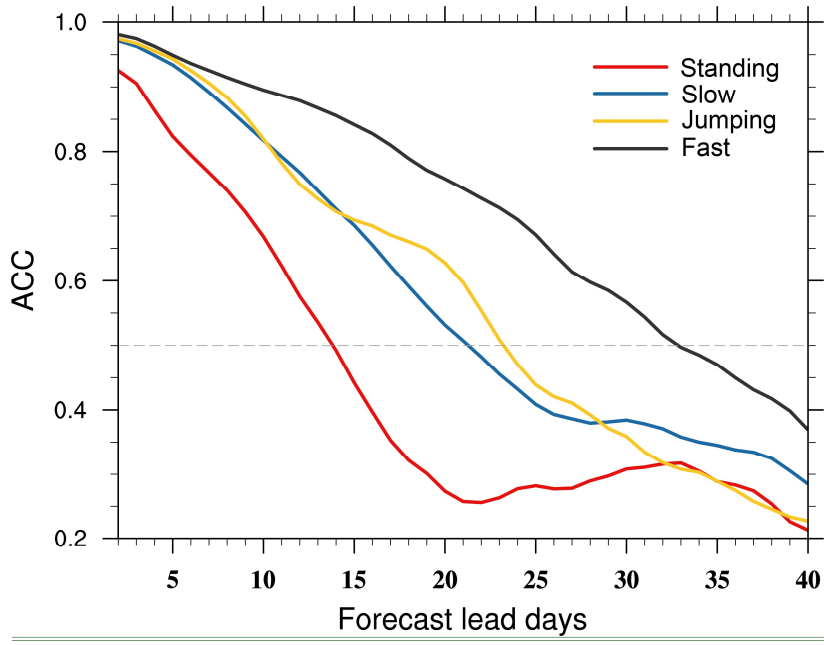
517

Figure 4. The ACC (a) varied with forecast lead days for initially strong (red) and weak (black) cases and (b) varied with forecast lag days for target strong (red) and weak (black) cases from the ensemble mean. The dashed lines in (a) and (b) have the values of 0.5. (c) The forecast of MJO amplitude varied with forecast lead days for initially strong cases from observation (black solid line), individual ensemble members of the model (red dashed line) and their ensemble mean (red solid line). (d) The forecast of MJO phase angle error (°) for initially strong cases (black solid line). The dashed line in (d) is the reference line with the values of 0.



518
519
520
521
522
523
524

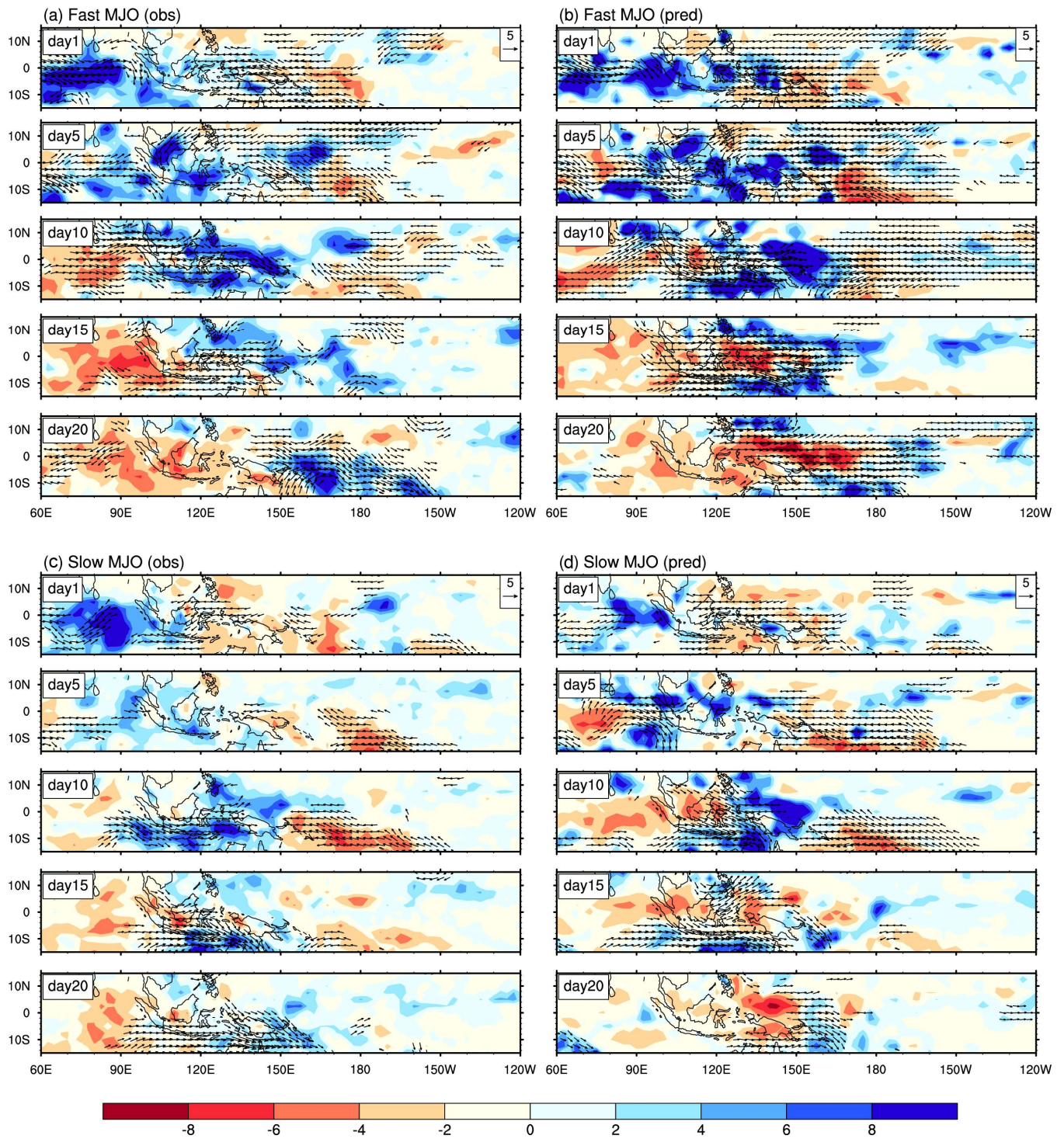
Figure 5. 10°S – 10°N averaged Precipitation anomalies (shading; mm day^{-1}) and 850-hPa zonal winds anomalies (contours with an interval of 1 m s^{-1}) varied with longitude (x-axis) and time lag (y-axis; days) composited for four types of the boreal winter MJO. The top row is for observation (NCEP winds and GPCP precipitation), and the bottom row is for model forecasts. The thin solid black lines represent positive values and the dashed lines represent negative values. The thick solid black line represents the propagation trajectory of the MJO, derived via least squares regression. The propagation speed of the propagating MJO is annotated in the top right corner of the panels.



525

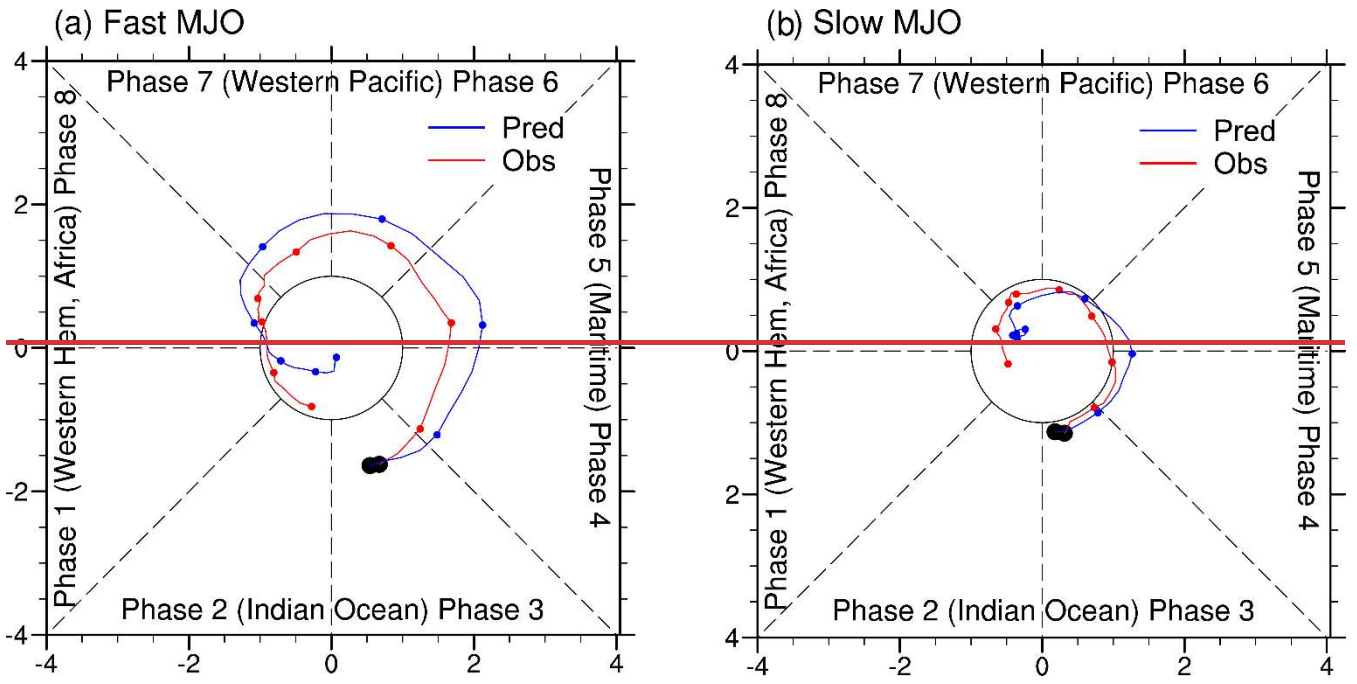
526 Figure A46. The bivariate ACC as a function of forecast lead days for fast, slow, jumping, and standing MJO events. The dashed
 527 line has the value of 0.5.

528



529
530
531
532

Figure 67. Evolution patterns of the composite precipitation (shading; mm day^{-1}) and 850-hPa winds (vectors; m s^{-1}) anomalies (exceeding 2 m/s) for day 1, day 5, day10, day15 and day 20 in (a) observed fast MJO, (b) simulated fast MJO, (c) observed slow MJO and (d) simulated slow MJO.

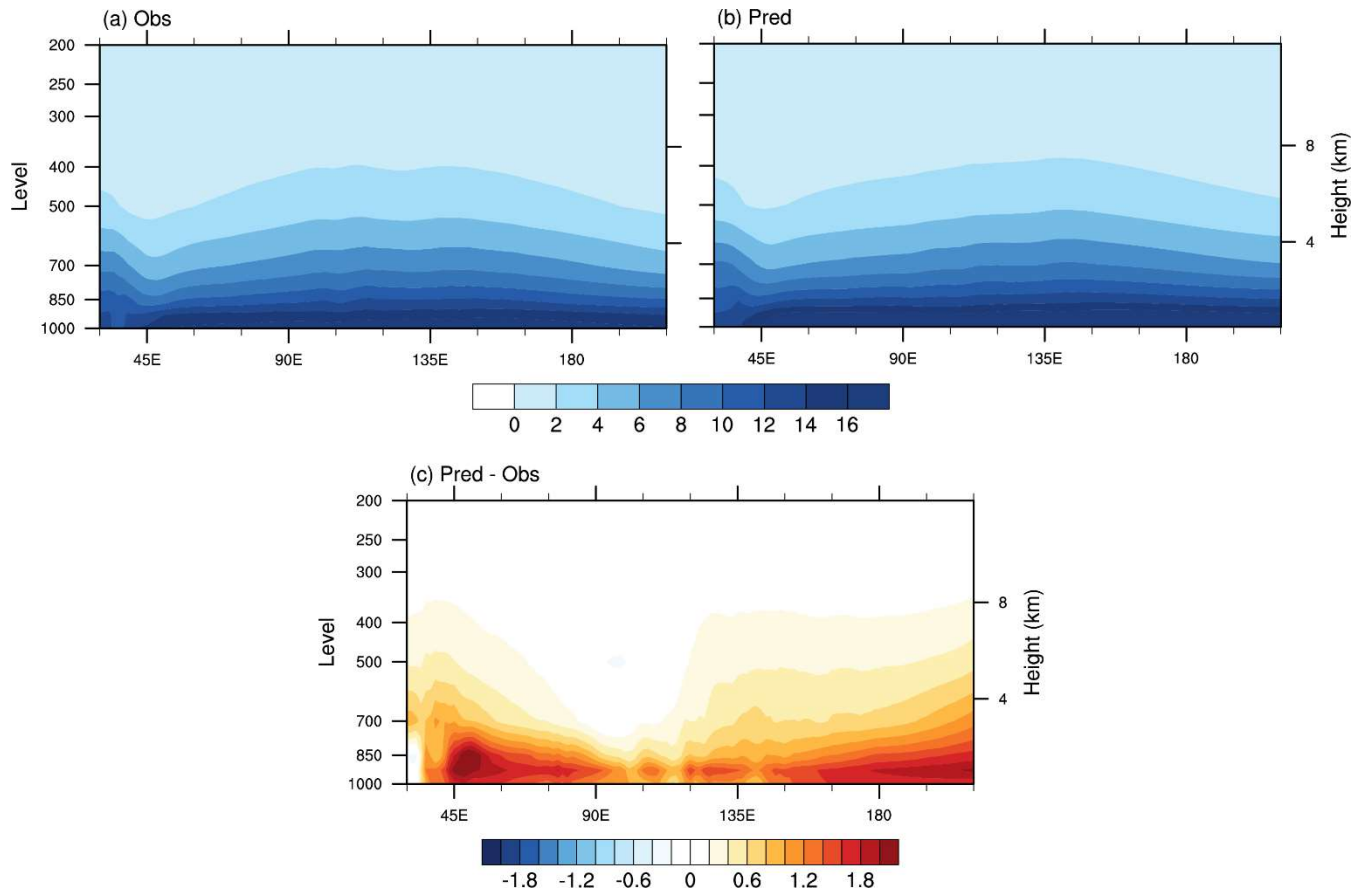


533

534

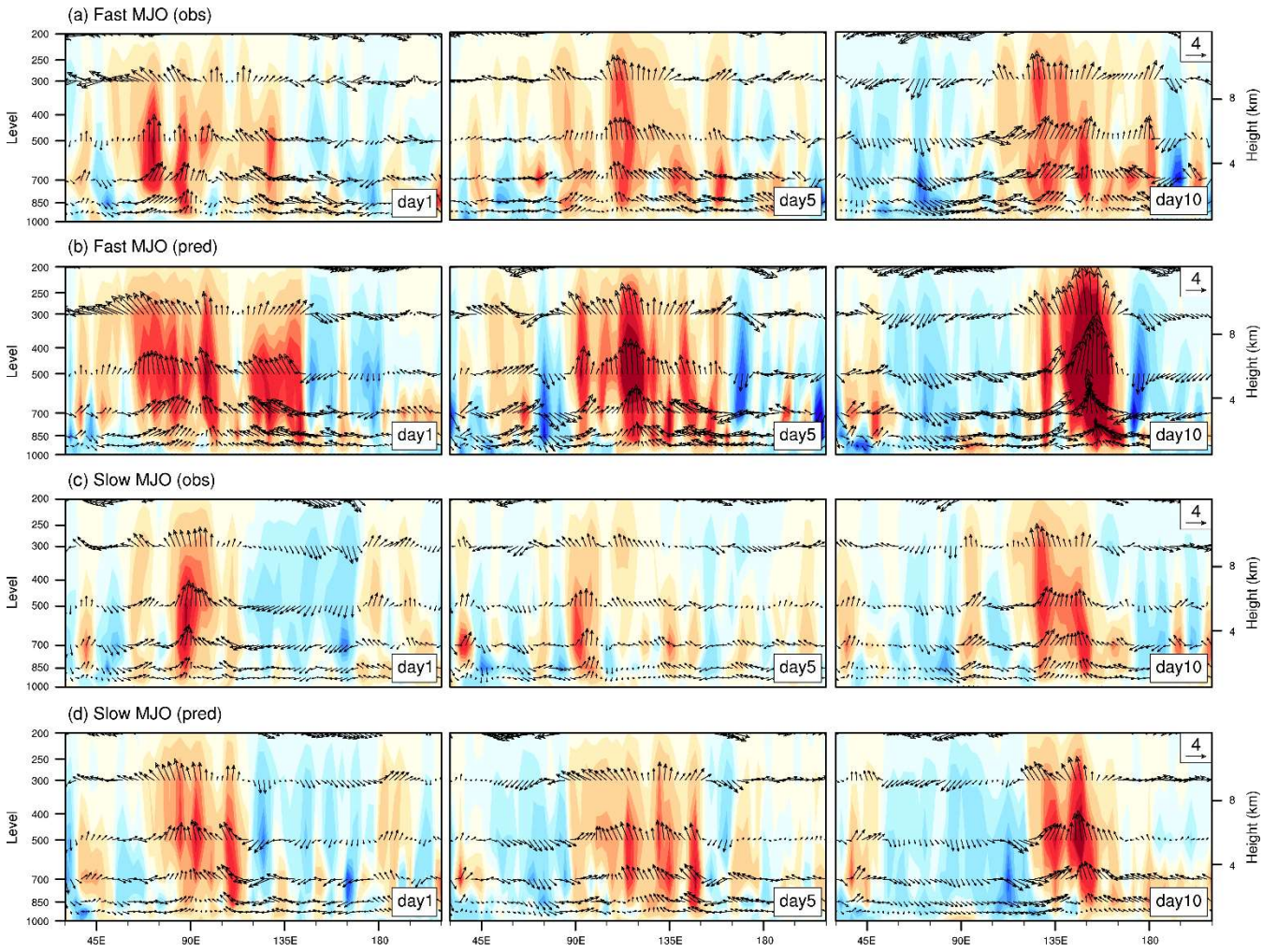
535

Figure 7. Composite phase diagrams for (a) fast MJO and (b) slow MJO events from observation (red lines) and IAP-CAS model (blue lines). The dots denote every 5 days from the forecast starting date.



536

537 **Figure 8. The longitude-vertical profiles of winter (November–April) mean specific humidity (g kg^{-1}) averaged over 10°S – 10°N for**
 538 **(a) observation, (b) IAP-CAS model, and (c) the difference between IAP-CAS model and observation.**



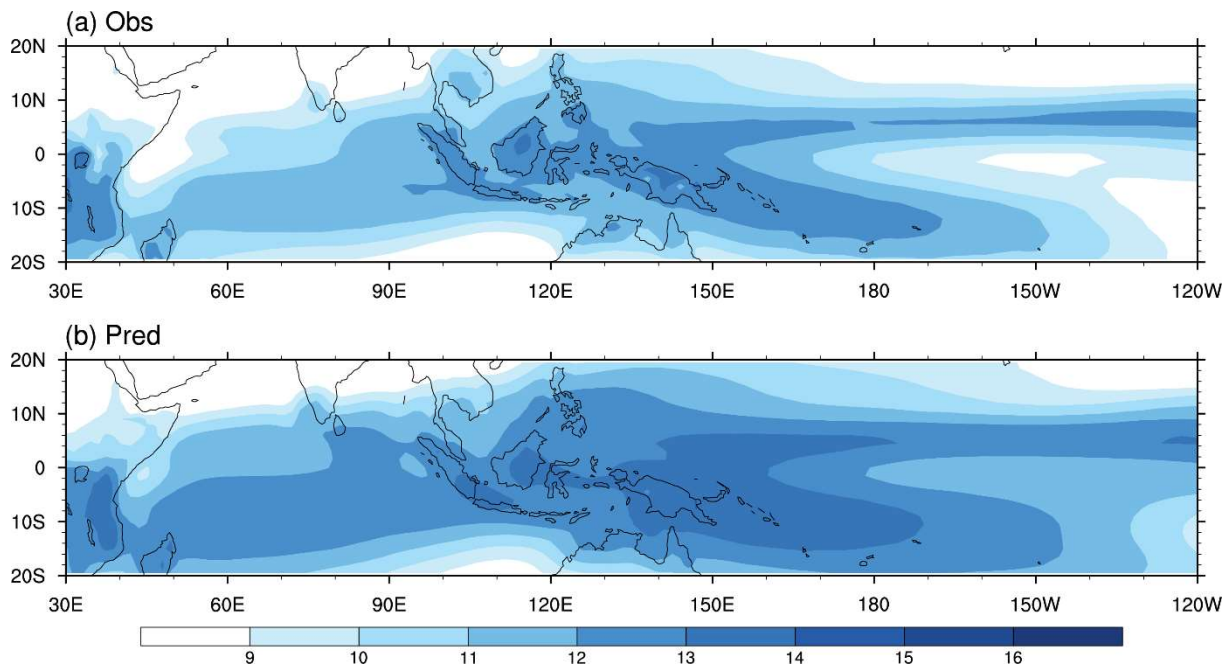
539

540

541

542

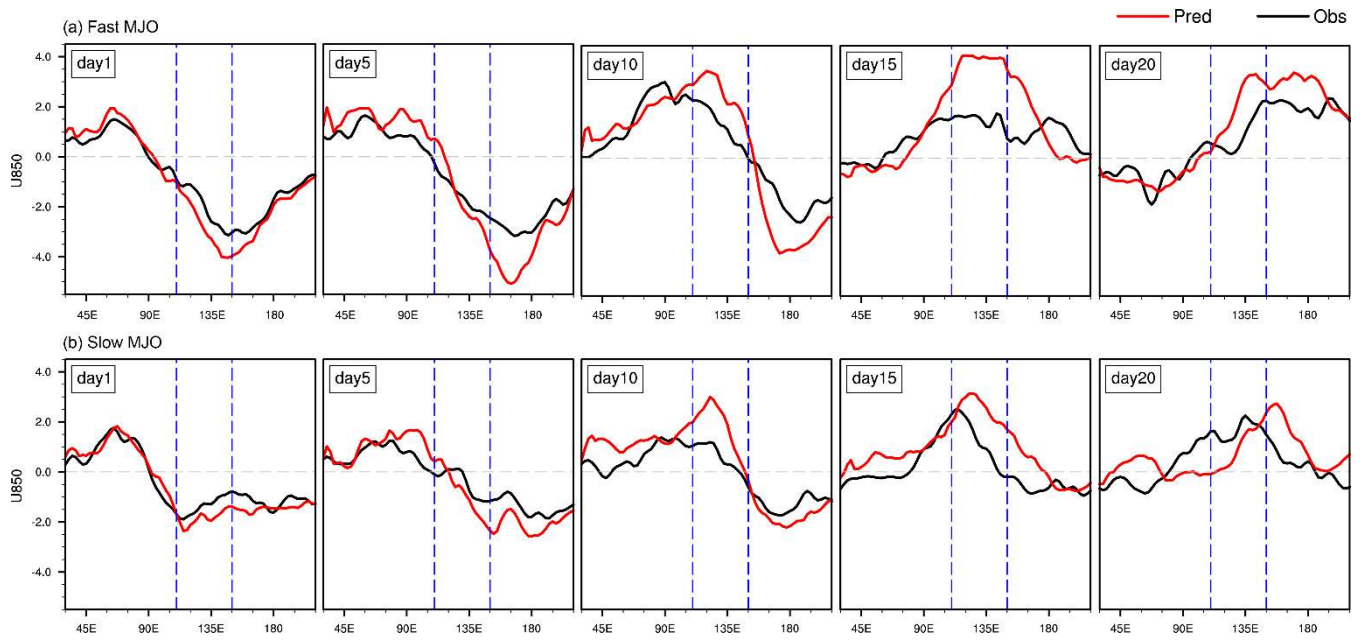
Figure 9. The composited longitude-vertical structure of precipitation heating (contours; $1 \times 10^{-2} \text{ J kg}^{-1} \text{ s}^{-1}$) and zonal and vertical winds anomalies (vectors; units are m/s for zonal winds and 0.01 Pa s^{-1} for vertical winds) averaged over $10^\circ \text{ S} - 10^\circ \text{ N}$ for day 1, day 5, day 10 in (a) observed fast MJO, (b) simulated fast MJO, (c) observed slow MJO and (d) simulated slow MJO.



543

544

Figure 10. The winter (November–April) mean specific humidity (g kg^{-1}) on 850hPa for (a) observation and (b) IAP-CAS model.



545

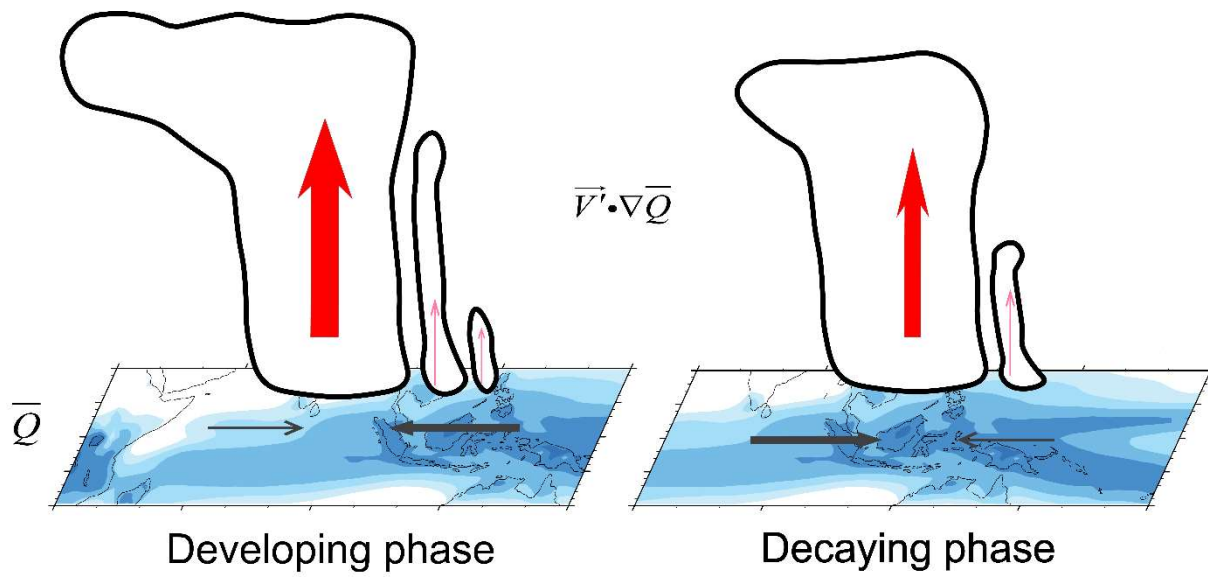
546

547

548

549

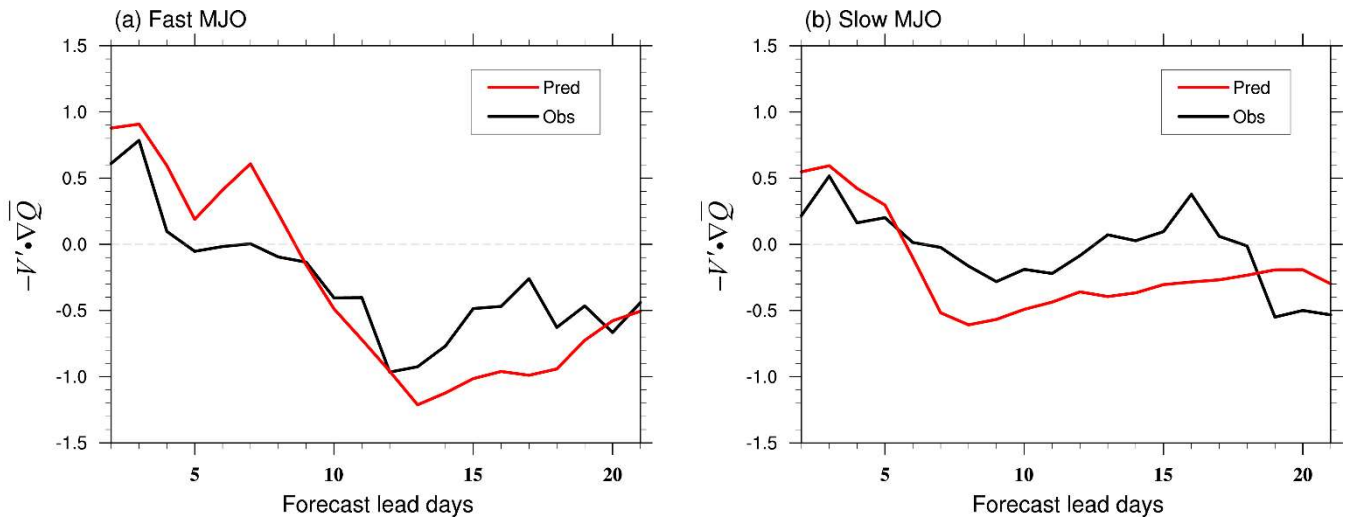
Figure 11. The composited longitudinal structure of the 850hPa zonal wind anomalies (m s^{-1}) averaged over 15°S – 15°N for day 1, day 5, day10, day15 and day 20 from observation (black solid line) and IAP-CAS model (red solid line) in fast and slow MJO events. The gray dashed line is the reference line with the values of 0. The two blue dashed lines are 110°E and 150°E respectively, which denote the extension of the MC region.



550

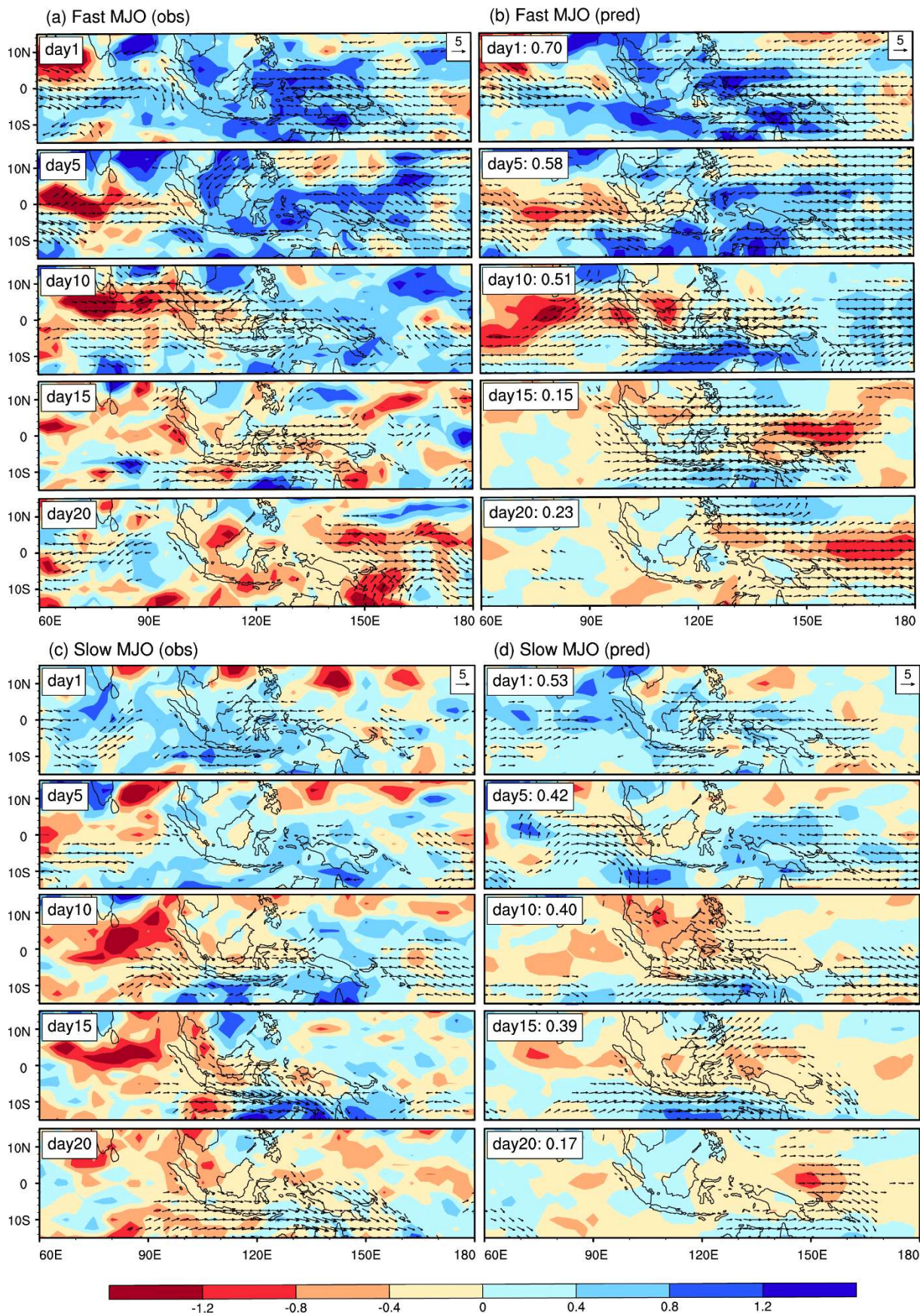
551

Figure 12. Schematic diagrams illustrating the moisture mode theory on MJO propagation in the MC region.



552

553 **Figure 13.** The composited $-V' \cdot \nabla \bar{Q}$ ($\text{g kg}^{-1} \text{s}^{-1}$) averaged over the MC region (15°S - 15°N , 110°E - 150°E) as a function of forecast
 554 lead days from observation (black solid line) and IAP-CAS model (red solid line) in (a) fast MJO and (b) slow MJO events. The gray
 555 dashed line is the reference line with the values of 0.



556
557
558
559
560

Figure 14. Evolution patterns of the composite specific humidity anomalies (g kg^{-1}) and winds (vectors; m s^{-1}) anomalies (exceeding 2 m/s) on 850hPa for day 1, day 5, day10, day15 and day 20 (a) observed fast MJO, (b) simulated fast MJO, (c) observed slow MJO and (d) simulated slow MJO. The spatial correlation coefficient between simulated and observed moisture anomalies is shown to the right of panels (b) and (c).

Table A12 Hybrid coefficient of hybrid sigma-pressure coordinates at layer interfaces in CAS FGOALS-f2

<u>Layer</u>	<u>Coefficient of pressure coordinates</u>	<u>The coefficient of sigma coordinates</u>	<u>Layer</u>	<u>Coefficient of pressure coordinates</u>	<u>The coefficient of sigma coordinates</u>
<u>1</u>	<u>100.00</u>	<u>0.00</u>	<u>18</u>	<u>27131.33</u>	<u>0.23</u>
<u>2</u>	<u>400.00</u>	<u>0.00</u>	<u>19</u>	<u>24406.11</u>	<u>0.32</u>
<u>3</u>	<u>818.60</u>	<u>0.00</u>	<u>20</u>	<u>21326.05</u>	<u>0.42</u>
<u>4</u>	<u>1378.89</u>	<u>0.00</u>	<u>21</u>	<u>18221.18</u>	<u>0.51</u>
<u>5</u>	<u>2091.80</u>	<u>0.00</u>	<u>22</u>	<u>15275.15</u>	<u>0.59</u>
<u>6</u>	<u>2983.64</u>	<u>0.00</u>	<u>23</u>	<u>12581.68</u>	<u>0.67</u>
<u>7</u>	<u>4121.79</u>	<u>0.00</u>	<u>24</u>	<u>10181.43</u>	<u>0.73</u>
<u>8</u>	<u>5579.22</u>	<u>0.00</u>	<u>25</u>	<u>8081.90</u>	<u>0.79</u>
<u>9</u>	<u>7419.79</u>	<u>0.00</u>	<u>26</u>	<u>6270.87</u>	<u>0.83</u>
<u>10</u>	<u>9704.83</u>	<u>0.00</u>	<u>27</u>	<u>4725.35</u>	<u>0.87</u>
<u>11</u>	<u>12496.34</u>	<u>0.00</u>	<u>28</u>	<u>3417.39</u>	<u>0.91</u>
<u>12</u>	<u>15855.26</u>	<u>0.00</u>	<u>29</u>	<u>2317.75</u>	<u>0.93</u>
<u>13</u>	<u>19839.62</u>	<u>0.00</u>	<u>30</u>	<u>1398.09</u>	<u>0.96</u>
<u>14</u>	<u>24502.73</u>	<u>0.00</u>	<u>31</u>	<u>632.50</u>	<u>0.98</u>
<u>15</u>	<u>28177.10</u>	<u>0.02</u>	<u>32</u>	<u>0.00</u>	<u>0.99</u>
<u>16</u>	<u>29525.28</u>	<u>0.06</u>	<u>33</u>	<u>0.00</u>	<u>1.00</u>
<u>17</u>	<u>29016.34</u>	<u>0.14</u>			

563

Table 3A2 Initialization information of the S2S ensemble forecast system

<u>Nudging type</u>	<u>Data Assimilation</u>	<u>Variable</u>	<u>Data</u>	<u>Frequency</u>
<u>Reanalysis nudging</u>	<u>Time-Lagged Nudging</u> (<u>Hoffman and Kalnay, 1983; Jeuken et al., 1996</u>)	<u>U, V, T, P_s, z_s^a</u> <u>SST</u>	<u>FNL (http://rda.ucar.edu/datasets/ds083.2, ds083.2 DOI: 10.5065/D6M043C6)</u> <u>NOAA OISST (Reynolds et al., 2007)</u>	<u>6h</u>
<u>Forecast nudging</u>		<u>U, V, T, P_s, z_s</u>	<u>GFS weather forecast</u>	<u>6h</u>

564

^a Table notes: U represents zonal wind, V represents meridional wind, T represents temperature, P_s represents surface pressure,

565

z_s represents surface geopotential height, and SST represents sea surface temperature.

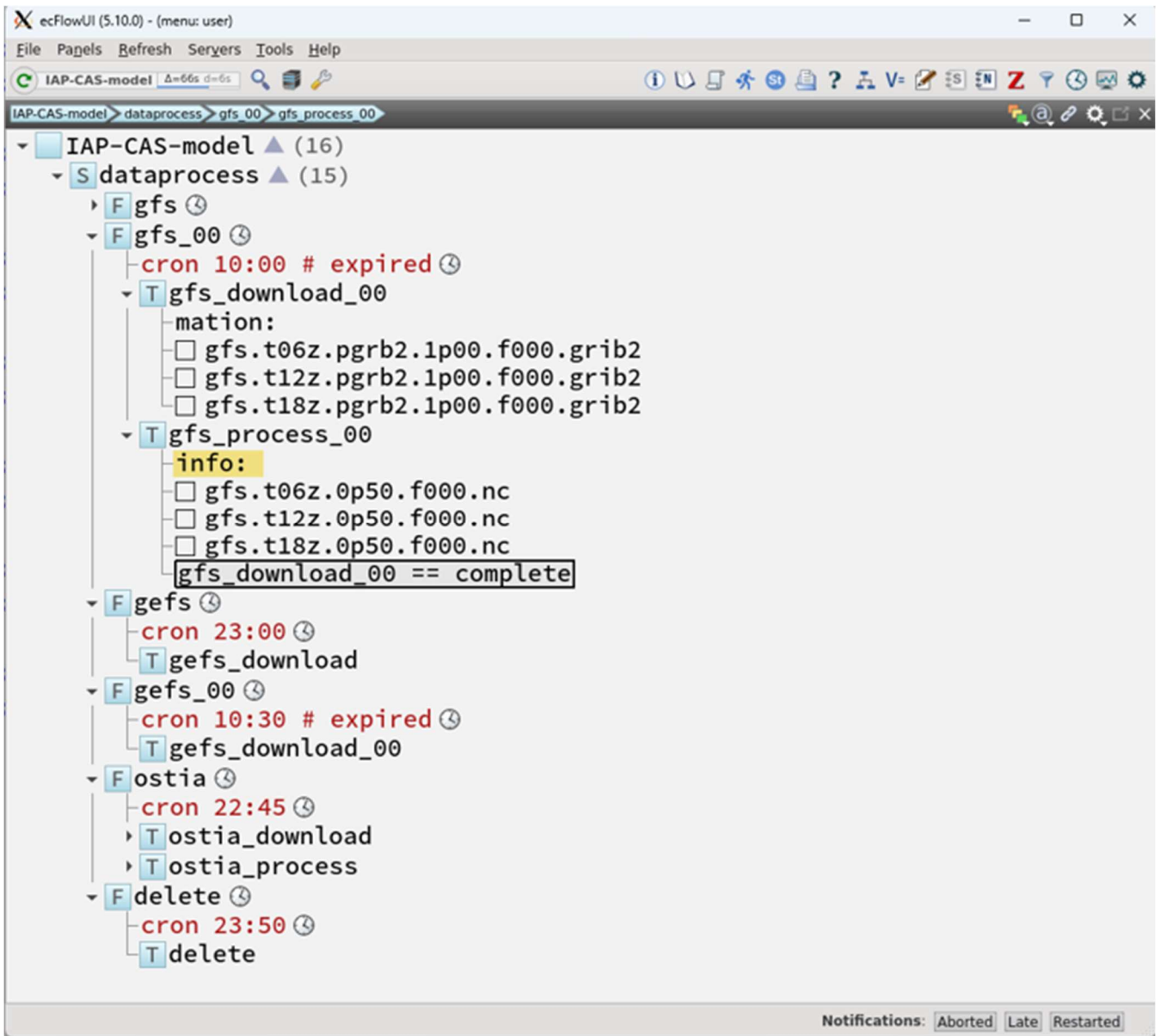
Table 4A3 Introduction to the output data of the S2S ensemble forecast system

<u>Experiment</u>	<u>Ensemble members</u>	<u>Time range</u>	<u>Frequency</u>	<u>Forecast time</u>	<u>Variable</u>	<u>Resolution</u>	<u>Interpolation method</u>
<u>Hindcast</u>	<u>4</u>	<u>1999-2018</u>	<u>Daily</u>	<u>65 days</u>	<u>25 variables</u>	<u>Horizontal:1.5°</u>	<u>One-order</u>
<u>Real-time forecast</u>	<u>16</u>	<u>2019</u>			<u>(A detailed list of variables is shown in Table-A4§)</u>	<u>×1.5°</u> <u>Vertical:7 levels</u> <u>(1000, 925, 850, 700, 500, 300, and 200hPa)</u>	<u>conservation</u>

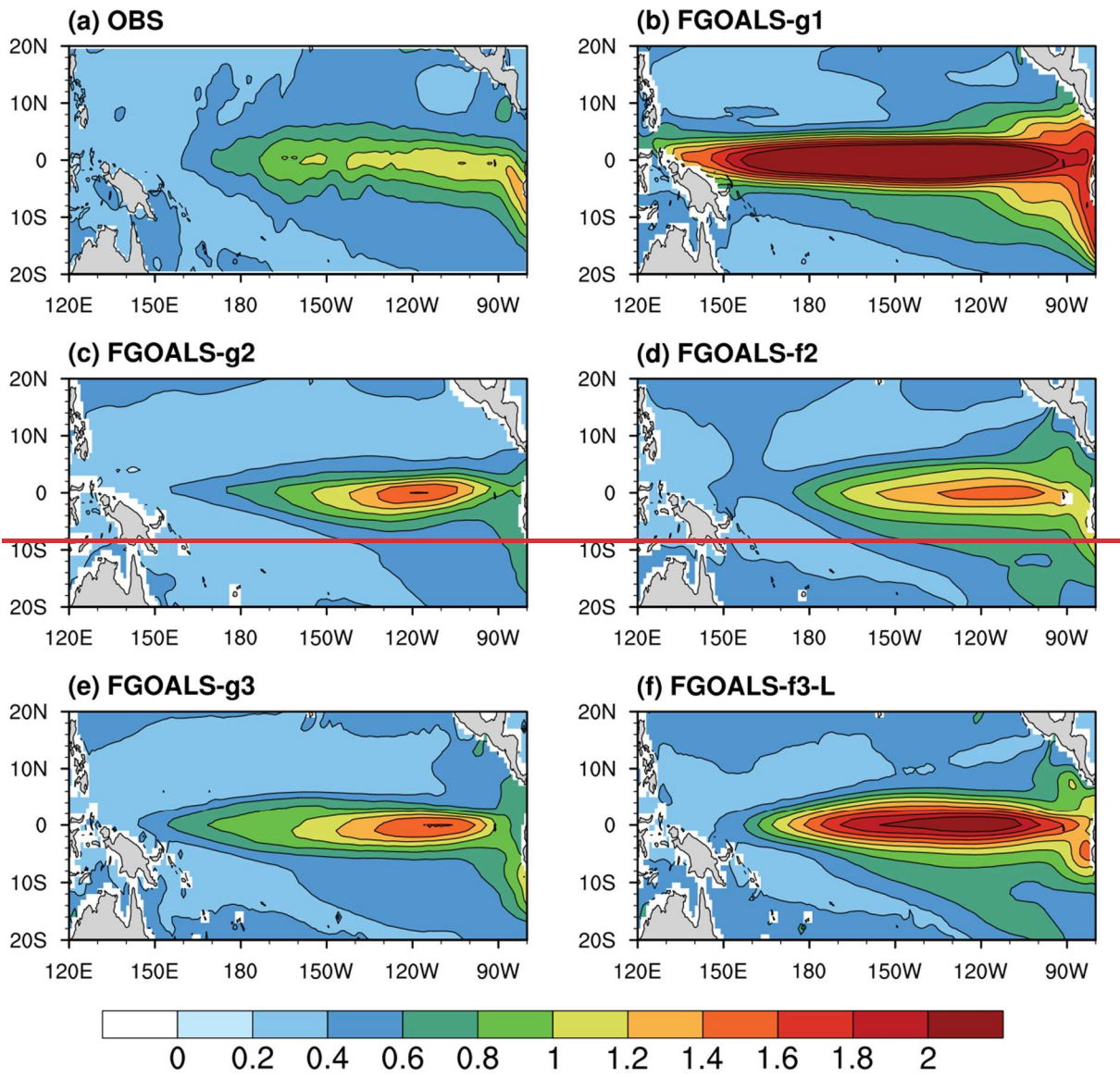
Table 5A4 List the output variables in the S2S ensemble forecast system

<u>Statistical process</u>	<u>Level(s)</u>	<u>Short name</u>	<u>Standard name</u>	<u>Unit</u>
<u>Instantaneous value/24h</u>	<u>The variables are located on 10 pressure layers (1000, 925, 850, 700, 500, 300, 200, 100, 50, 10 hPa)</u>	<u>gh</u>	<u>Geopotential height</u>	<u>gpm</u>
		<u>t</u>	<u>Temperature</u>	<u>K</u>
		<u>u</u>	<u>U-velocity</u>	<u>m s⁻¹</u>
		<u>v</u>	<u>V-velocity</u>	<u>m s⁻¹</u>
		<u>w</u>	<u>Vertical velocity</u>	<u>pa s⁻¹</u>
<u>2-dimensional variables</u>	<u>The variable is located on 7 pressure layers (1000, 925, 850, 700, 500, 300, 200 hPa)</u>	<u>q</u>	<u>Specific humidity</u>	<u>kg kg⁻¹</u>
		<u>w</u>	<u>Vertical velocity</u>	<u>pa s⁻¹</u>
		<u>sp</u>	<u>Surface pressure</u>	<u>Pa</u>
<u>Daily average value</u>		<u>lsm</u>	<u>Land sea mask</u>	<u>Proportion of land</u>
		<u>orog</u>	<u>Orography</u>	<u>gpm</u>
		<u>tcc</u>	<u>Total cloud cover</u>	<u>%</u>
		<u>skt</u>	<u>Skin temperature</u>	<u>K</u>
		<u>2t</u>	<u>Surface air temperature</u>	<u>K</u>
		<u>2d</u>	<u>Surface air dewpoint temperature</u>	<u>2d</u>
		<u>wtmp</u>	<u>Sea surface temperature</u>	<u>K</u>
<u>ci</u>	<u>Sea ice cover</u>	<u>proportion</u>		

<u>24-hour</u>	<u>sf</u>	<u>Snow fall water equivalent</u>	<u>kg m⁻²</u>
<u>accumulated</u>	<u>ttr</u>	<u>Time-integrated top net thermal radiation</u>	<u>W m⁻²s</u>
<u>value</u>	<u>ssr</u>	<u>Time-integrated surface net solar radiation</u>	<u>W m⁻²s</u>
	<u>str</u>	<u>Time-integrated surface net thermal radiation</u>	<u>W m⁻²s</u>
	<u>ssrd</u>	<u>Time-integrated surface solar radiation downwards</u>	<u>W m⁻²s</u>
	<u>strd</u>	<u>Time-integrated surface thermal radiation downwards</u>	<u>W m⁻²s</u>
<u>Instantaneous</u>	<u>mx2t6</u>	<u>Surface air maximum temperature</u>	<u>K</u>
<u>value/6h</u>	<u>mn2t6</u>	<u>Surface air minimum temperature</u>	<u>K</u>
	<u>10u</u>	<u>10 metre u-velocity</u>	<u>m s⁻¹</u>
	<u>10v</u>	<u>10 metre v-velocity</u>	<u>m s⁻¹</u>
<u>6-hour</u>	<u>tp</u>	<u>Total precipitation</u>	<u>kg m⁻²</u>
<u>accumulated</u>			
<u>value</u>			



569
 570 **Figure A1.** The structure of ecFlow (ECMWF Workflow). EcFlow, developed and maintained by the ECMWF, is a client/server
 571 workflow package designed to facilitate the execution of a substantial number of programs within a controlled environment. It is
 572 used in the IAP-CAS model to accomplish the download and preprocessing of the forcing data.

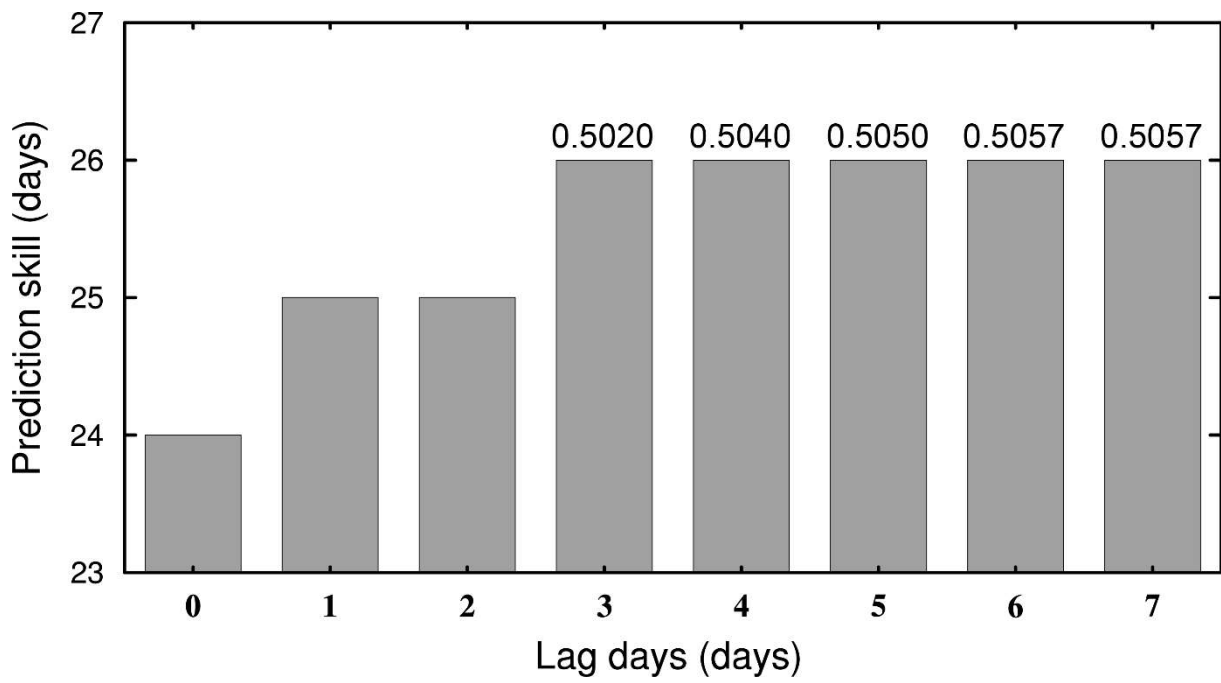


573

574

575

Figure A2. The horizontal distribution of Sea Surface Temperature Anomaly (SSTA) standard deviations in (a) observation and (b)-(e) five FGOALS models from 1948 to 2018.



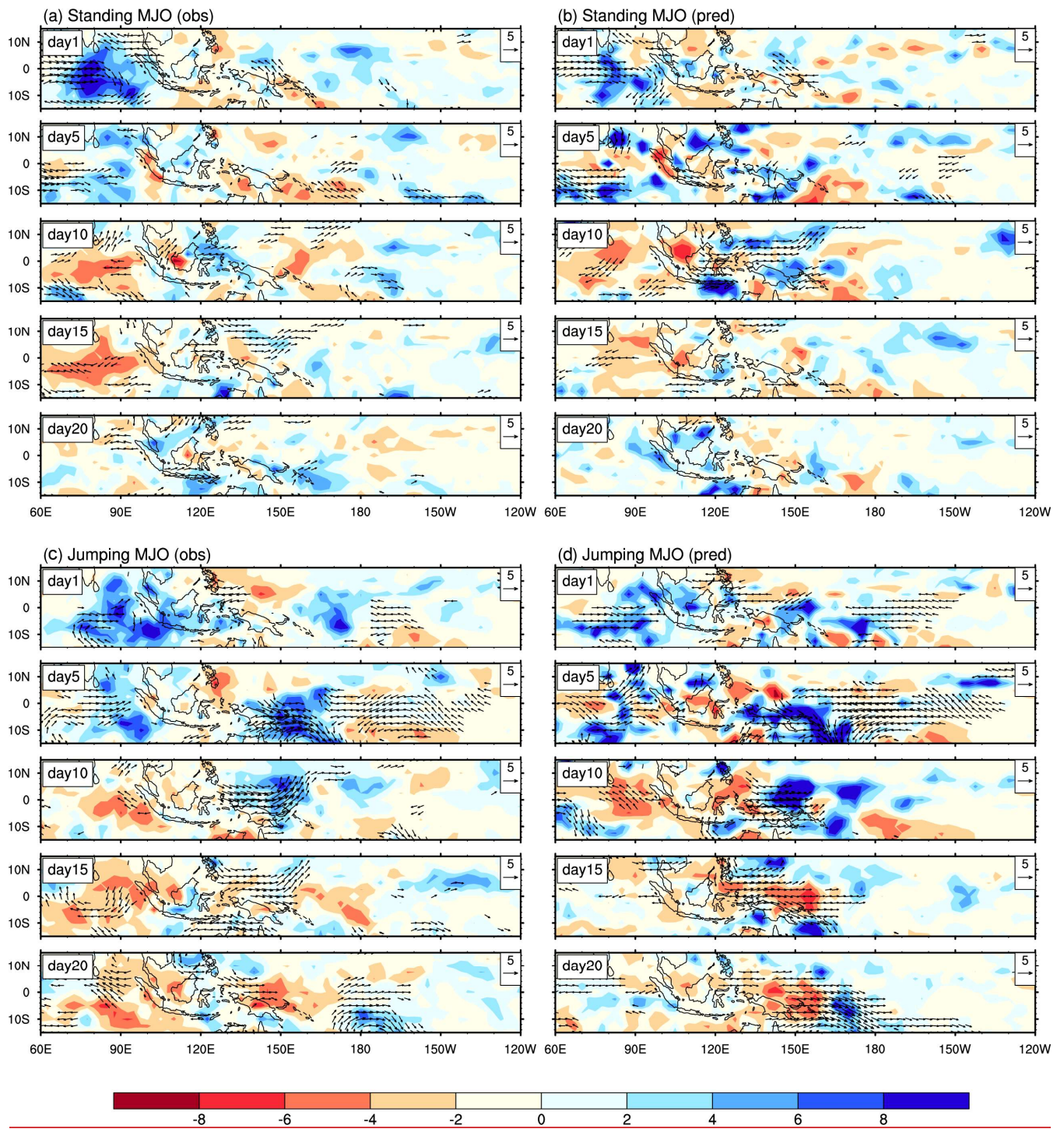
576

577

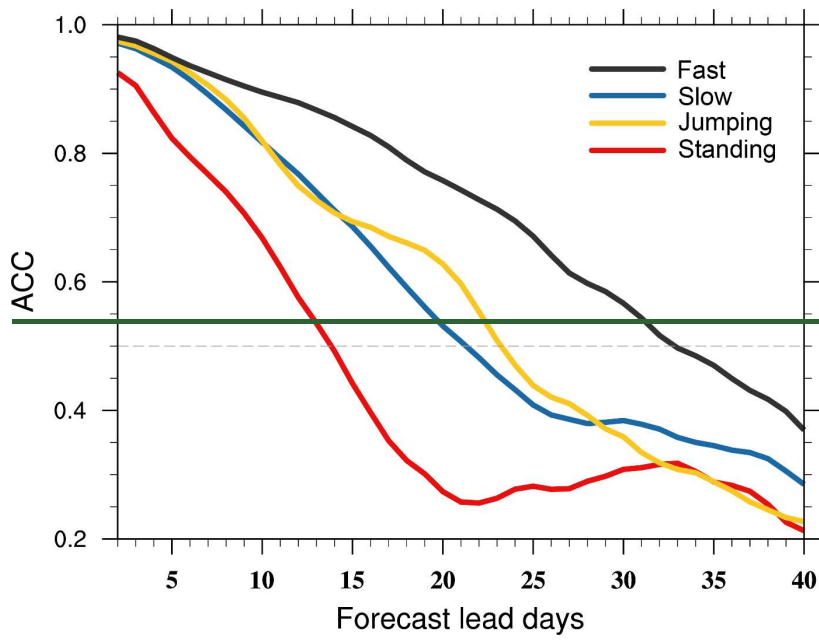
578

579

Figure A3A2. MJO forecast skill of the ensemble mean of time-lagged members as a function of lag days. The values on the bars represent the ACC on day 26.



580
 581 **Figure A3. Evolution patterns of the composite precipitation (shading; mm day⁻¹) and 850-hPa winds (vectors; m s⁻¹) anomalies**
 582 **(exceeding 2 m/s) for day 1, day 5, day10, day15 and day 20 in (a) observed standing MJO, (b) simulated standing MJO, (c) observed**
 583 **Jumping MJO and (d) simulated Jumping MJO.**

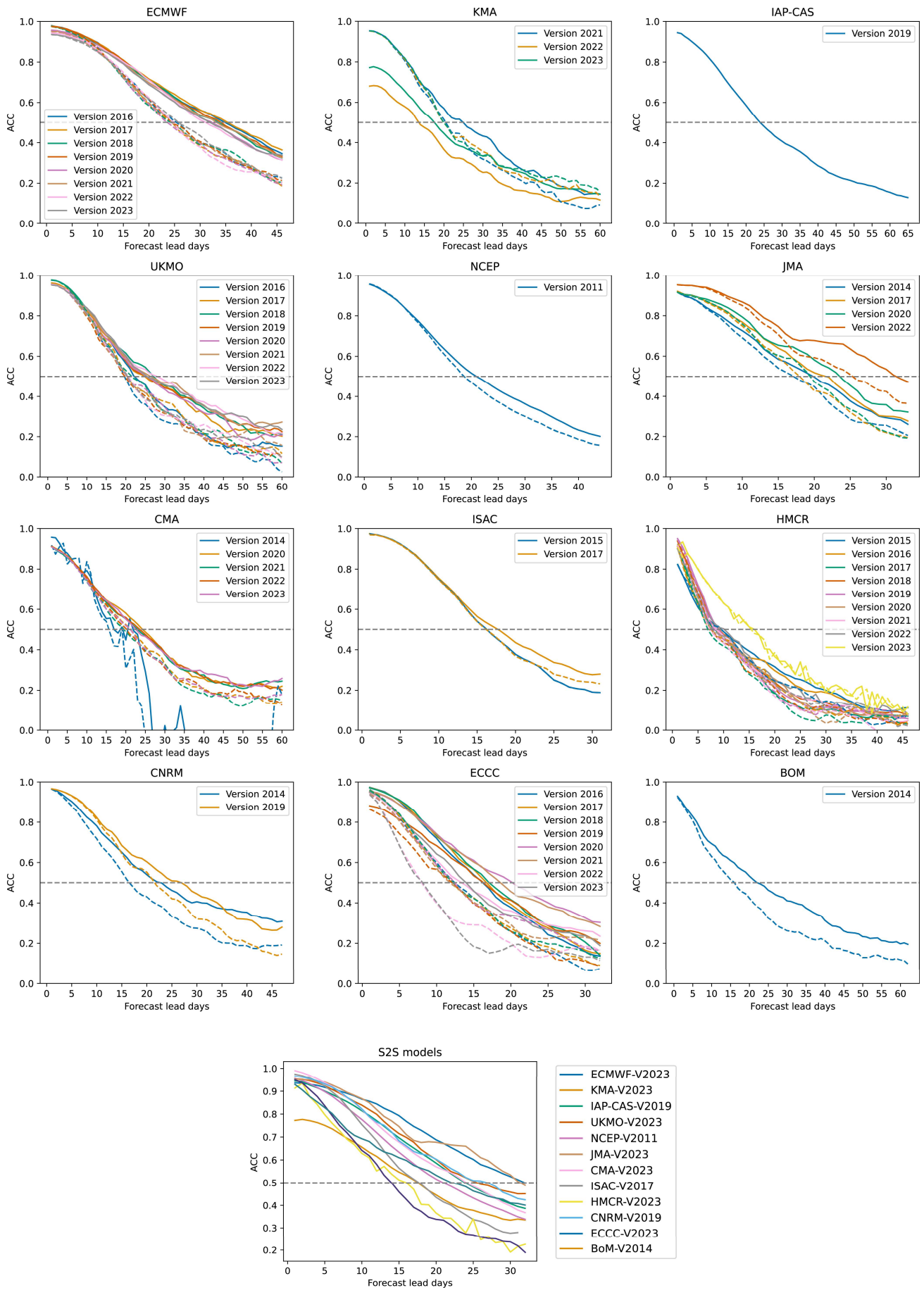


584

585

586

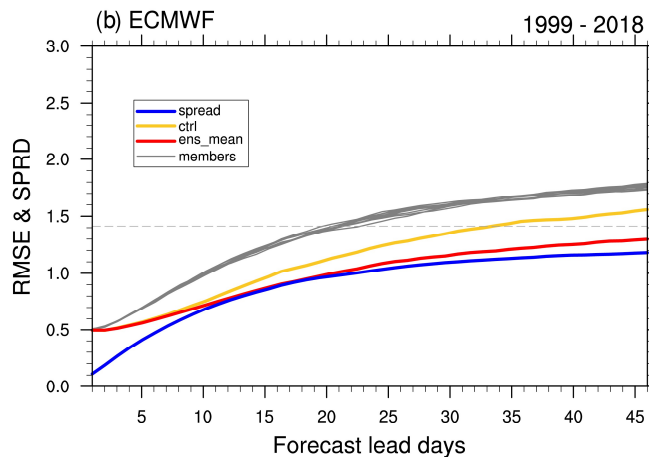
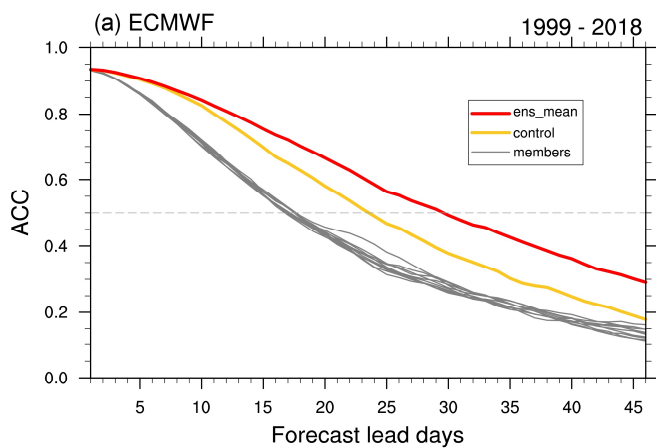
Figure A4. The bivariate ACC as a function of forecast lead days for fast, slow, jumping, and standing MJO events. The dashed line has the value of 0.5.



587
588
589
590
591

Figure A4. The MJO forecast skill of 12 S2S models, providing comparisons between various model versions over the years, and the latest versions of 12 models. The evaluation covers the period from 2001 to 2010, except for CMA, which spans from 2008 to 2013. The solid lines represent the skill of ensemble mean forecasts, while the dashed lines represent the skill of deterministic forecasts.
Figure A5. MJO forecast skill of S2S models. (a) The ACC between the model ensemble means and ERA-Interim over 10 year (2001-

592 ~~2010) RMM index for 11 S2S models. The datasets used in this study are from the following versions (with the year of update as the~~
593 ~~version number): IAP-2022, BoM-2014, CNRM-2019, ECCO-2022, ECMWF-2022, HMCR-2022, ISAC-2017, JMA-2020, NCEP-~~
594 ~~2011, UKMO-2022, CMA-2022. (b) The ACC and (c) the RMSE from individual members (gray solid line), ensemble ctrl (green~~
595 ~~solid line), and 10-member ensemble mean (red solid line) as a function of forecast lead days. The blue solid line denotes the ensemble~~
596 ~~spread. The dashed line in (a) and (b) has the values of 0.5, and it represents 1.414 in (c).~~



597 **Figure A5. The ACC (a) and the RMSE (b) of ECMWF (2019 version) from individual members (gray solid line), ensemble ctrl**
 598 **(yellow solid line), and 10-member ensemble mean (red solid line) as a function of forecast lead days. The blue solid line denotes the**
 599 **ensemble spread. The dashed line in (a) has a value of 0.5, and it represents 1.414 in (b).**
 600

597
598
599
600
601

602 **Code availability**

603 The code of the IAP-CAS model is archived on Zenodo (<https://doi.org/10.5281/zenodo.10791355>). The code used to
604 reproduce the figures in this work can be obtained from <https://doi.org/10.5281/zenodo.10817813>.

605 **Data availability**

606 The boundary conditions and input data are available at <https://doi.org/10.5281/zenodo.10820243>. The data for initial
607 ization in the IAP-CAS S2S system is available at <http://rda.ucar.edu/datasets/ds083.2>, ds083.2[DOI: 10.5065/D6M043-
608 C6 (FNL), <https://www.ncei.noaa.gov/products/optimum-interpolation-sst> (NOAA OISST) and [https://www.ncei.noaa.gov/
609 v/products/weather-climate-models/global-forecast](https://www.ncei.noaa.gov/products/weather-climate-models/global-forecast) (GFS weather forecast). The hindcast dataset of the IAP-CAS S2S
610 system used in the article is publicly available on the three S2S Data Portals (ECMWF: [https://apps.ecmwf.int/data-
611 sets/](https://apps.ecmwf.int/datasets/); CMA: <http://s2s.cma.cn/index>; IRI: <https://iridl.ldeo.columbia.edu/SOURCES/ECMWF/S2S/>). All the validation
612 data are available to download from the cited references or data links shown in Section 3.1.

613 **Author contribution**

614 Q.B. led the IAP-CAS model development. All other co-authors contributed to it. B.H. and X.F.W. designed the experiments
615 and carried them out. Y.K.L. utilized the dataset to assess the performance of the IAP-CAS S2S system and wrote the final
616 document with contributions from all other authors. Q.B. reviewed and edited the manuscript. G.X.W., Y.M.L., and J.Y.
617 supervised and supported this research and gave important opinions.

618 **Competing interests**

619 The authors declare no conflict of interest.

620 **Acknowledgments**

621 This work was supported by funding from the National Natural Science Foundation of China (Grant 42175161, 42261144671),
622 ~~and~~ the Alliance of International Science Organizations (Grant ANSO-CR-KP-2020-01), and the National Key Scientific and
623 Technological Infrastructure project “Earth System Numerical Simulation Facility”.

624 **References**

625 Adames, Á. F. and Kim, D.: The MJO as a Dispersive, Convectively Coupled Moisture Wave: Theory and Observations,
626 Journal of the Atmospheric Sciences, 73, 913–941, <https://doi.org/10.1175/JAS-D-15-0170.1>, 2016.

627 Adames, Á. F. and Wallace, J. M.: Three-Dimensional Structure and Evolution of the MJO and Its Relation to the Mean Flow,
628 *Journal of the Atmospheric Sciences*, 71, 2007–2026, <https://doi.org/10.1175/JAS-D-13-0254.1>, 2014.

629 Adames, Á. F. and Wallace, J. M.: Three-Dimensional Structure and Evolution of the Moisture Field in the MJO, *Journal of*
630 *the Atmospheric Sciences*, 72, 3733–3754, <https://doi.org/10.1175/JAS-D-15-0003.1>, 2015.

631 Adler, R. F., Huffman, G. J., Chang, A., Ferraro, R., Xie, P.-P., Janowiak, J., Rudolf, B., Schneider, U., Curtis, S., Bolvin, D.,
632 Gruber, A., Susskind, J., Arkin, P., and Nelkin, E.: The Version-2 Global Precipitation Climatology Project (GPCP) Monthly
633 Precipitation Analysis (1979–Present), *Journal of Hydrometeorology*, 4, 1147–1167, [https://doi.org/10.1175/1525-7541\(2003\)004<1147:TVGPCP>2.0.CO;2](https://doi.org/10.1175/1525-7541(2003)004<1147:TVGPCP>2.0.CO;2), 2003.

635 Ahn, M., Kim, D., Kang, D., Lee, J., Sperber, K. R., Gleckler, P. J., Jiang, X., Ham, Y., and Kim, H.: MJO Propagation Across
636 the Maritime Continent: Are CMIP6 Models Better Than CMIP5 Models?, *Geophysical Research Letters*, 47,
637 <https://doi.org/10.1029/2020GL087250>, 2020.

638 Ahn, M. S., Kim, D., Kang, D., Lee, J., Sperber, K. R., and Gleckler, P. J.: MJO Simulation in CMIP6 Models: How much
639 improvement has been made from CMIP5 to CMIP6?, 2019, A41G-04, 2019.

640 Bao, Q.: Outlook for El Niño and the Indian Ocean Dipole in autumn-winter 2018–2019, *CSB*, 73–78,
641 <https://doi.org/10.1360/N972018-00913>, 2019.

642 Bao, Q. and Li, J.: Progress in climate modeling of precipitation over the Tibetan Plateau, *National Science Review*, 7, 486–
643 487, <https://doi.org/10.1093/nsr/nwaa006>, 2020.

644 Bao, Q., Liu, Y., Wu, G., He, B., Li, J., Wang, L., Wu, X., Chen, K., Wang, X., Yang, J., and Zhang, X.: CAS FGOALS-f3-
645 H and CAS FGOALS-f3-L outputs for the high-resolution model intercomparison project simulation of CMIP6, *Atmospheric*
646 *and Oceanic Science Letters*, 13, 576–581, <https://doi.org/10.1080/16742834.2020.1814675>, 2020.

647 Benedict, J. J. and Randall, D. A.: Observed Characteristics of the MJO Relative to Maximum Rainfall, *Journal of the*
648 *Atmospheric Sciences*, 64, 2332–2354, <https://doi.org/10.1175/JAS3968.1>, 2007.

649 Bessafi, M. and Wheeler, M. C.: Modulation of south Indian ocean tropical cyclones by the Madden-Julian oscillation and
650 convectively coupled equatorial waves, *Mon. Weather Rev.*, 134, 638–656, <https://doi.org/10.1175/MWR3087.1>, 2006.

651 Cassou, C.: Intraseasonal interaction between the Madden–Julian Oscillation and the North Atlantic Oscillation, *Nature*, 455,
652 523–527, <https://doi.org/10.1038/nature07286>, 2008.

653 Chen, G., Ling, J., Zhang, R., Xiao, Z., and Li, C.: The MJO From CMIP5 to CMIP6: Perspectives From Tracking MJO
654 Precipitation, *Geophysical Research Letters*, 49, <https://doi.org/10.1029/2021GL095241>, 2022.

655 Craig, A. P., Vertenstein, M., and Jacob, R.: A new flexible coupler for earth system modeling developed for CCSM4 and
656 CESM1, *The International Journal of High Performance Computing Applications*, 26, 31–42,
657 <https://doi.org/10.1177/1094342011428141>, 2012.

658 Crueger, T., Stevens, B., and Brokopf, R.: The Madden-Julian Oscillation in ECHAM6 and the Introduction of an Objective
659 MJO Metric, *J. Clim.*, 26, 3241–3257, <https://doi.org/10.1175/JCLI-D-12-00413.1>, 2013.

660 DeMott, C. A., Wolding, B. O., Maloney, E. D., and Randall, D. A.: Atmospheric Mechanisms for MJO Decay Over the
661 Maritime Continent, *Journal of Geophysical Research: Atmospheres*, 123, 5188–5204, <https://doi.org/10.1029/2017JD026979>,
662 2018.

663 ERA, C.: Fifth generation of ECMWF atmospheric reanalyses of the global climate, Copernicus Climate Change Service
664 Climate Data Store (CDS), 2017.

665 Ferreira, R. N., Schubert, W. H., and Hack, J. J.: Dynamical aspects of twin tropical cyclones associated with the Madden-
666 Julian oscillation, *J. Atmos. Sci.*, 53, 929–945, [https://doi.org/10.1175/1520-0469\(1996\)053<0929:DAOTTC>2.0.CO;2](https://doi.org/10.1175/1520-0469(1996)053<0929:DAOTTC>2.0.CO;2), 1996.

667 Gonzalez, A. O. and Jiang, X.: Winter mean lower tropospheric moisture over the Maritime Continent as a climate model
668 diagnostic metric for the propagation of the Madden-Julian oscillation, *Geophysical Research Letters*, 44, 2588–2596,
669 <https://doi.org/10.1002/2016GL072430>, 2017.

670 Goswami, B. N.: South asian monsoon, Springer, 2012.

671 Gottschalck, J., Wheeler, M., Weickmann, K., Vitart, F., Savage, N., Lin, H., Hendon, H., Waliser, D., Sperber, K., Nakagawa,
672 M., Prestrelo, C., Flatau, M., and Higgins, W.: A Framework for Assessing Operational Madden–Julian Oscillation Forecasts:
673 A CLIVAR MJO Working Group Project, *Bull. Amer. Meteor. Soc.*, 91, 1247–1258,
674 <https://doi.org/10.1175/2010BAMS2816.1>, 2010.

675 Hall, J. D., Matthews, A. J., and Karoly, D. J.: The modulation of tropical cyclone activity in the Australian region by the
676 Madden-Julian oscillation, *Mon. Weather Rev.*, 129, 2970–2982, [https://doi.org/10.1175/1520-0493\(2001\)129<2970:TMOTCA>2.0.CO;2](https://doi.org/10.1175/1520-0493(2001)129<2970:TMOTCA>2.0.CO;2), 2001.

677

678 Hannah, W. M., Maloney, E. D., and Pritchard, M. S.: Consequences of systematic model drift in DYNAMO MJO hindcasts
679 with SP-CAM and CAM5, *Journal of Advances in Modeling Earth Systems*, 7, 1051–1074,
680 <https://doi.org/10.1002/2014MS000423>, 2015.

681 Harris, L., Zhou, L., Lin, S.-J., Chen, J.-H., Chen, X., Gao, K., Morin, M., Rees, S., Sun, Y., Tong, M., Xiang, B., Bender, M.,
682 Benson, R., Cheng, K.-Y., Clark, S., Elbert, O. D., Hazelton, A., Huff, J. J., Kaltenbaugh, A., Liang, Z., Marchok, T., Shin, H.
683 H., and Stern, W.: GFDL SHIELD: A Unified System for Weather-to-Seasonal Prediction, *Journal of Advances in Modeling*
684 *Earth Systems*, 12, e2020MS002223, <https://doi.org/10.1029/2020MS002223>, 2020.

685 Harris, L. M. and Lin, S.-J.: A Two-Way Nested Global-Regional Dynamical Core on the Cubed-Sphere Grid, *Monthly*
686 *Weather Review*, 141, 283–306, <https://doi.org/10.1175/MWR-D-11-00201.1>, 2013.

687 Hendon, H. H. and Salby, M. L.: The Life Cycle of the Madden–Julian Oscillation, *Journal of the Atmospheric Sciences*, 51,
688 2225–2237, [https://doi.org/10.1175/1520-0469\(1994\)051<2225:TLCOTM>2.0.CO;2](https://doi.org/10.1175/1520-0469(1994)051<2225:TLCOTM>2.0.CO;2), 1994.

689 Ho, C.-H., Kim, J.-H., Jeong, J.-H., Kim, H.-S., and Chen, D.: Variation of tropical cyclone activity in the South Indian Ocean:
690 El Niño–Southern Oscillation and Madden-Julian Oscillation effects, *J. Geophys. Res.*, 111, D22101,
691 <https://doi.org/10.1029/2006JD007289>, 2006.

692 Hoffman, R. N. and Kalnay, E.: Lagged average forecasting, an alternative to Monte Carlo forecasting, *Tellus A: Dynamic*
693 *Meteorology and Oceanography*, 35, 100–118, <https://doi.org/10.3402/tellusa.v35i2.11425>, 1983.

694 Hsu, H. H. and Lee, M. Y.: Topographic effects on the eastward propagation and initiation of the Madden-Julian oscillation,
695 *J. Clim.*, 18, 795–809, <https://doi.org/10.1175/JCLI-3292.1>, 2005.

696 Hsu, H.-H.: Intraseasonal variability of the atmosphere–ocean–climate system: East Asian monsoon, in: *Intraseasonal*
697 *Variability in the Atmosphere-Ocean Climate System*, edited by: Lau, W. K.-M. and Waliser, D. E., Springer Berlin Heidelberg,
698 Berlin, Heidelberg, 73–110, https://doi.org/10.1007/978-3-642-13914-7_3, 2012.

699 Hsu, P. and Li, T.: Role of the Boundary Layer Moisture Asymmetry in Causing the Eastward Propagation of the Madden–
700 Julian Oscillation, *Journal of Climate*, 25, 4914–4931, <https://doi.org/10.1175/JCLI-D-11-00310.1>, 2012.

701 Hung, M.-P., Lin, J.-L., Wang, W., Kim, D., Shinoda, T., and Weaver, S. J.: MJO and Convectively Coupled Equatorial Waves
702 Simulated by CMIP5 Climate Models, *Journal of Climate*, 26, 6185–6214, <https://doi.org/10.1175/JCLI-D-12-00541.1>, 2013.

703 Hunke, E. C., Lipscomb, W. H., Turner, A. K., Jeffery, N., and Elliott, S.: Cice: the los alamos sea ice model documentation
704 and software user’s manual version 4.1 la-cc-06-012, T-3 Fluid Dynamics Group, Los Alamos National Laboratory, 675, 500,
705 2010.

706 Inness, P. M. and Slingo, J. M.: The interaction of the Madden-Julian Oscillation with the Maritime Continent in a GCM, *Q.*
707 *J. R. Meteorol. Soc.*, 132, 1645–1667, <https://doi.org/10.1256/qj.05.102>, 2006.

708 Jeuken, A. B. M., Siegmund, P. C., Heijboer, L. C., Feichter, J., and Bengtsson, L.: On the potential of assimilating
709 meteorological analyses in a global climate model for the purpose of model validation, *Journal of Geophysical Research:*
710 *Atmospheres*, 101, 16939–16950, <https://doi.org/10.1029/96JD01218>, 1996.

711 Jiang, X.: Key processes for the eastward propagation of the Madden-Julian Oscillation based on multimodel simulations: Key
712 Model Processes for MJO Propagation, *J. Geophys. Res. Atmos.*, 122, 755–770, <https://doi.org/10.1002/2016JD025955>, 2017.

713 Jiang, X., Adames, Á. F., Zhao, M., Waliser, D., and Maloney, E.: A Unified Moisture Mode Framework for Seasonality of
714 the Madden–Julian Oscillation, *Journal of Climate*, 31, 4215–4224, <https://doi.org/10.1175/JCLI-D-17-0671.1>, 2018.

715 Kanamitsu, M., Ebisuzaki, W., Woollen, J., Yang, S.-K., Hnilo, J. J., Fiorino, M., and Potter, G. L.: NCEP–DOE AMIP-II
716 Reanalysis (R-2), *Bulletin of the American Meteorological Society*, 83, 1631–1644, [https://doi.org/10.1175/BAMS-83-11-](https://doi.org/10.1175/BAMS-83-11-1631)
717 1631, 2002.

718 Kemball-Cook, S. R. and Weare, B. C.: The Onset of Convection in the Madden–Julian Oscillation, *J. Climate*, 14, 780–793,
719 [https://doi.org/10.1175/1520-0442\(2001\)014<0780:TOOCIT>2.0.CO;2](https://doi.org/10.1175/1520-0442(2001)014<0780:TOOCIT>2.0.CO;2), 2001.

720 Kerbyson, D. J. and Jones, P. W.: A Performance Model of the Parallel Ocean Program, *The International Journal of High*
721 *Performance Computing Applications*, 19, 261–276, <https://doi.org/10.1177/1094342005056114>, 2005.

722 Kim, D., Kug, J.-S., and Sobel, A. H.: Propagating versus Nonpropagating Madden–Julian Oscillation Events, *Journal of*
723 *Climate*, 27, 111–125, <https://doi.org/10.1175/JCLI-D-13-00084.1>, 2014a.

724 Kim, H.: MJO Propagation Processes and Mean Biases in the SubX and S2S Reforecasts, *J. Geophys. Res. Atmos.*, 124, 9314–
725 9331, <https://doi.org/10.1029/2019JD031139>, 2019.

726 Kim, H., Vitart, F., and Waliser, D. E.: Prediction of the Madden–Julian Oscillation: A Review, *J Climate*, 31, 9425–9443,
727 <https://doi.org/10.1175/JCLI-D-18-0210.1>, 2018.

728 Kim, H.-M.: The impact of the mean moisture bias on the key physics of MJO propagation in the ECMWF reforecast, *Journal*
729 *of Geophysical Research: Atmospheres*, 122, 7772–7784, <https://doi.org/10.1002/2017JD027005>, 2017.

730 Kim, H.-M., Webster, P. J., Toma, V. E., and Kim, D.: Predictability and Prediction Skill of the MJO in Two Operational
731 Forecasting Systems, *J Climate*, 27, 5364–5378, <https://doi.org/10.1175/JCLI-D-13-00480.1>, 2014b.

732 Lau, K.-M. and Chan, P. H.: Aspects of the 40–50 Day Oscillation during the Northern Summer as Inferred from Outgoing
733 Longwave Radiation, *Monthly Weather Review*, 114, 1354–1367, [https://doi.org/10.1175/1520-0493\(1986\)114<1354:AOTDOD>2.0.CO;2](https://doi.org/10.1175/1520-0493(1986)114<1354:AOTDOD>2.0.CO;2), 1986.

734

735 Lau, W. K., Waliser, D. E., and Lau, W. K.: *El Nino southern oscillation connection*, Springer, 2005.

736 Lawrence, D. M., Oleson, K. W., Flanner, M. G., Thornton, P. E., Swenson, S. C., Lawrence, P. J., Zeng, X., Yang, Z.-L.,
737 Levis, S., Sakaguchi, K., Bonan, G. B., and Slater, A. G.: Parameterization improvements and functional and structural
738 advances in Version 4 of the Community Land Model: PARAMETERIZATION IMPROVEMENTS AND FUNCTIONAL
739 AND STRUCTURAL ADVANCES, *J. Adv. Model. Earth Syst.*, 3, n/a-n/a, <https://doi.org/10.1029/2011MS00045>, 2011.

740 Leutbecher, M. and Palmer, T. N.: Ensemble forecasting, *Journal of Computational Physics*, 227, 3515–3539,
741 <https://doi.org/10.1016/j.jcp.2007.02.014>, 2008.

742 Li, J., Bao, Q., Liu, Y., Wu, G., Wang, L., He, B., Wang, X., and Li, J.: Evaluation of FAMIL2 in Simulating the Climatology
743 and Seasonal-to-Interannual Variability of Tropical Cyclone Characteristics, *J. Adv. Model. Earth Syst.*, 11, 1117–1136,
744 <https://doi.org/10.1029/2018MS001506>, 2019.

745 Liebmann, B. and Smith, C. A.: Description of a Complete (Interpolated) Outgoing Longwave Radiation Dataset, *Bulletin of*
746 *the American Meteorological Society*, 77, 1275–1277, 1996.

747 Liebmann, B., Hendon, H., and Glick, J.: The Relationship Between Tropical Cyclones of the Western Pacific and Indian
748 Oceans and the Madden-Julian Oscillation, *J. Meteorol. Soc. Jpn.*, 72, 401–412, https://doi.org/10.2151/jmsj1965.72.3_401,
749 1994.

750 Lim, Y., Son, S.-W., and Kim, D.: MJO Prediction Skill of the Subseasonal-to-Seasonal Prediction Models, *Journal of Climate*,
751 31, 4075–4094, <https://doi.org/10.1175/JCLI-D-17-0545.1>, 2018.

752 Lin, H., Brunet, G., and Derome, J.: Forecast Skill of the Madden–Julian Oscillation in Two Canadian Atmospheric Models,
753 Monthly Weather Review, 136, 4130–4149, <https://doi.org/10.1175/2008MWR2459.1>, 2008.

754 Lin, S.-J.: A “Vertically Lagrangian” Finite-Volume Dynamical Core for Global Models, Monthly Weather Review, 132,
755 2293–2307, [https://doi.org/10.1175/1520-0493\(2004\)132<2293:AVLFDC>2.0.CO;2](https://doi.org/10.1175/1520-0493(2004)132<2293:AVLFDC>2.0.CO;2), 2004.

756 Lin, Y., Farley, R., and Orville, H.: Bulk Parameterization of the Snow Field in a Cloud Model, JOURNAL OF CLIMATE
757 AND APPLIED METEOROLOGY, 22, 1065–1092, [https://doi.org/10.1175/1520-0450\(1983\)022<1065:BPOTSF>2.0.CO;2](https://doi.org/10.1175/1520-0450(1983)022<1065:BPOTSF>2.0.CO;2),
758 1983.

759 Liu, F., Wang, B., Ouyang, Y., Wang, H., Qiao, S., Chen, G., and Dong, W.: Intraseasonal variability of global land monsoon
760 precipitation and its recent trend, npj Clim Atmos Sci, 5, 30, <https://doi.org/10.1038/s41612-022-00253-7>, 2022.

761 Liu, Y. Q.: Prediction of monthly-seasonal precipitation using coupled SVD patterns between soil moisture and subsequent
762 precipitation, Geophys. Res. Lett., 30, 1827, <https://doi.org/10.1029/2003GL017709>, 2003.

763 Lorenz, E. N.: Predictability: A problem partly solved, in Proceedings of Seminar on Predictability, 4–8 September 1995, 1996.

764 Madden, R. A. and Julian, P. R.: Detection of a 40–50 Day Oscillation in the Zonal Wind in the Tropical Pacific, Journal of
765 the Atmospheric Sciences, 28, 702–708, [https://doi.org/10.1175/1520-0469\(1971\)028<0702:DOADOI>2.0.CO;2](https://doi.org/10.1175/1520-0469(1971)028<0702:DOADOI>2.0.CO;2), 1971.

766 Maloney, E. D.: An Intraseasonal Oscillation Composite Life Cycle in the NCAR CCM3.6 with Modified Convection, J.
767 Climate, 15, 964–982, [https://doi.org/10.1175/1520-0442\(2002\)015<0964:AIOCLC>2.0.CO;2](https://doi.org/10.1175/1520-0442(2002)015<0964:AIOCLC>2.0.CO;2), 2002.

768 Maloney, E. D. and Hartmann, D. L.: Modulation of eastern North Pacific hurricanes by the Madden-Julian oscillation, J.
769 Clim., 13, 1451–1460, [https://doi.org/10.1175/1520-0442\(2000\)013<1451:MOENPH>2.0.CO;2](https://doi.org/10.1175/1520-0442(2000)013<1451:MOENPH>2.0.CO;2), 2000.

770 Mu, M., Duan, W. S., and Wang, B.: Conditional nonlinear optimal perturbation and its applications, Nonlinear Processes in
771 Geophysics, 10, 493–501, <https://doi.org/10.5194/npg-10-493-2003>, 2003.

772 Nasuno, T., Li, T., and Kikuchi, K.: Moistening Processes before the Convective Initiation of Madden–Julian Oscillation
773 Events during the CINDY2011/DYNAMO Period, Monthly Weather Review, 143, 622–643, [https://doi.org/10.1175/MWR-](https://doi.org/10.1175/MWR-D-14-00132.1)
774 [D-14-00132.1](https://doi.org/10.1175/MWR-D-14-00132.1), 2015.

775 Neena, J. M., Lee, J. Y., Waliser, D., Wang, B., and Jiang, X.: Predictability of the Madden–Julian Oscillation in the
776 Intraseasonal Variability Hindcast Experiment (ISVHE)*, J Climate, 27, 4531–4543, [https://doi.org/10.1175/JCLI-D-13-](https://doi.org/10.1175/JCLI-D-13-00624.1)
777 [00624.1](https://doi.org/10.1175/JCLI-D-13-00624.1), 2014.

778 Nerger, L., Tang, Q., and Mu, L.: Efficient ensemble data assimilation for coupled models with the Parallel Data Assimilation
779 Framework: example of AWI-CM (AWI-CM-PDAF 1.0), Geosci. Model Dev., 13, 4305–4321, [https://doi.org/10.5194/gmd-](https://doi.org/10.5194/gmd-13-4305-2020)
780 [13-4305-2020](https://doi.org/10.5194/gmd-13-4305-2020), 2020.

781 Oleson, W., Lawrence, M., Bonan, B., Flanner, G., Kluzek, E., Lawrence, J., Levis, S., Swenson, C., Thornton, E., Dai, A.,
782 Decker, M., Dickinson, R., Feddema, J., Heald, L., Hoffman, F., Lamarque, J.-F., Mahowald, N., Niu, G.-Y., Qian, T.,

783 Randerson, J., Running, S., Sakaguchi, K., Slater, A., Stockli, R., Wang, A., Yang, Z.-L., Zeng, X., and Zeng, X.: Technical
784 Description of version 4.0 of the Community Land Model (CLM), <https://doi.org/10.5065/D6FB50WZ>, 2010.

785 Park, S. and Bretherton, C. S.: The University of Washington Shallow Convection and Moist Turbulence Schemes and Their
786 Impact on Climate Simulations with the Community Atmosphere Model, *J. Clim.*, 22, 3449–3469,
787 <https://doi.org/10.1175/2008JCLI2557.1>, 2009.

788 Pham, D. T.: Stochastic Methods for Sequential Data Assimilation in Strongly Nonlinear Systems, *Mon. Wea. Rev.*, 129,
789 1194–1207, [https://doi.org/10.1175/1520-0493\(2001\)129<1194:SMFSDA>2.0.CO;2](https://doi.org/10.1175/1520-0493(2001)129<1194:SMFSDA>2.0.CO;2), 2001.

790 Putman, W. M. and Lin, S.-J.: Finite-volume transport on various cubed-sphere grids, *Journal of Computational Physics*, 227,
791 55–78, <https://doi.org/10.1016/j.jcp.2007.07.022>, 2007.

792 Rashid, H. A., Hendon, H. H., Wheeler, M. C., and Alves, O.: Prediction of the Madden–Julian oscillation with the POAMA
793 dynamical prediction system, *Clim Dynam*, 36, 649–661, <https://doi.org/10.1007/s00382-010-0754-x>, 2011.

794 Raymond, D. J. and Fuchs, Ž.: Moisture Modes and the Madden–Julian Oscillation, *Journal of Climate*, 22, 3031–3046,
795 <https://doi.org/10.1175/2008JCLI2739.1>, 2009.

796 Reynolds, R. W., Smith, T. M., Liu, C., Chelton, D. B., Casey, K. S., and Schlax, M. G.: Daily High-Resolution-Blended
797 Analyses for Sea Surface Temperature, *Journal of Climate*, 20, 5473–5496, <https://doi.org/10.1175/2007JCLI1824.1>, 2007.

798 Rousseeuw, P.: Silhouettes - a Graphical Aid to the Interpretation and Validation of Cluster-Analysis, *J. Comput. Appl. Math.*,
799 20, 53–65, [https://doi.org/10.1016/0377-0427\(87\)90125-7](https://doi.org/10.1016/0377-0427(87)90125-7), 1987.

800 Rui, H. and Wang, B.: Development Characteristics and Dynamic Structure of Tropical Intraseasonal Convection Anomalies,
801 *Journal of the Atmospheric Sciences*, 47, 357–379, [https://doi.org/10.1175/1520-0469\(1990\)047<0357:DCADSO>2.0.CO;2](https://doi.org/10.1175/1520-0469(1990)047<0357:DCADSO>2.0.CO;2),
802 1990a.

803 Rui, H. and Wang, B.: Development Characteristics and Dynamic Structure of Tropical Intraseasonal Convection Anomalies,
804 *Journal of the Atmospheric Sciences*, 47, 357–379, [https://doi.org/10.1175/1520-0469\(1990\)047<0357:DCADSO>2.0.CO;2](https://doi.org/10.1175/1520-0469(1990)047<0357:DCADSO>2.0.CO;2),
805 1990b.

806 Vitart, F.: Madden—Julian Oscillation prediction and teleconnections in the S2S database, *Q.J.R. Meteorol. Soc.*, 143, 2210–
807 2220, <https://doi.org/10.1002/qj.3079>, 2017.

808 Vitart, F. and Molteni, F.: Dynamical Extended-Range Prediction of Early Monsoon Rainfall over India, *Mon. Weather Rev.*,
809 137, 1480–1492, <https://doi.org/10.1175/2008MWR2761.1>, 2009.

810 Vitart, F. and Molteni, F.: Simulation of the Madden-Julian Oscillation and its teleconnections in the ECMWF forecast system,
811 *Q. J. R. Meteorol. Soc.*, 136, 842–855, <https://doi.org/10.1002/qj.623>, 2010.

812 Vitart, F., Ardilouze, C., Bonet, A., Brookshaw, A., Chen, M., Codorean, C., Déqué, M., Ferranti, L., Fucile, E., Fuentes, M.,
813 Hendon, H., Hodgson, J., Kang, H.-S., Kumar, A., Lin, H., Liu, G., Liu, X., Malguzzi, P., Mallas, I., Manoussakis, M.,
814 Mastrangelo, D., MacLachlan, C., McLean, P., Minami, A., Mladek, R., Nakazawa, T., Najm, S., Nie, Y., Rixen, M., Robertson,

815 A. W., Ruti, P., Sun, C., Takaya, Y., Tolstykh, M., Venuti, F., Waliser, D., Woolnough, S., Wu, T., Won, D.-J., Xiao, H.,
816 Zaripov, R., and Zhang, L.: The Subseasonal to Seasonal (S2S) Prediction Project Database, *B Am Meteorol Soc*, 98, 163–
817 173, <https://doi.org/10.1175/BAMS-D-16-0017.1>, 2017.

818 Waliser, D. E., Lau, K. M., Stern, W., and Jones, C.: Potential Predictability of the Madden–Julian Oscillation, *B Am Meteorol*
819 *Soc*, 84, 33–50, <https://doi.org/10.1175/BAMS-84-1-33>, 2003.

820 Wang, B.: Dynamics of Tropical Low-Frequency Waves: An Analysis of the Moist Kelvin Wave, *Journal of the Atmospheric*
821 *Sciences*, 45, 2051–2065, [https://doi.org/10.1175/1520-0469\(1988\)045<2051:DOTLFW>2.0.CO;2](https://doi.org/10.1175/1520-0469(1988)045<2051:DOTLFW>2.0.CO;2), 1988.

822 Wang, B. and Lee, S.-S.: MJO Propagation Shaped by Zonal Asymmetric Structures: Results from 24 GCM Simulations,
823 *Journal of Climate*, 30, 7933–7952, <https://doi.org/10.1175/JCLI-D-16-0873.1>, 2017.

824 Wang, B., Chen, G., and Liu, F.: Diversity of the Madden-Julian Oscillation, *SCIENCE ADVANCES*, 2019.

825 Wang, W., Hung, M.-P., Weaver, S. J., Kumar, A., and Fu, X.: MJO prediction in the NCEP Climate Forecast System version
826 2, *Clim Dyn*, 42, 2509–2520, <https://doi.org/10.1007/s00382-013-1806-9>, 2014.

827 Wheeler, M. C. and Hendon, H. H.: An All-Season Real-Time Multivariate MJO Index: Development of an Index for
828 Monitoring and Prediction, *Monthly Weather Review*, 132, 1917–1932, [https://doi.org/10.1175/1520-0493\(2004\)132<1917:AARMMI>2.0.CO;2](https://doi.org/10.1175/1520-0493(2004)132<1917:AARMMI>2.0.CO;2), 2004a.

830 Wheeler, M. C. and Hendon, H. H.: An All-Season Real-Time Multivariate MJO Index: Development of an Index for
831 Monitoring and Prediction, *Mon. Wea. Rev.*, 132, 1917–1932, [https://doi.org/10.1175/1520-0493\(2004\)132<1917:AARMMI>2.0.CO;2](https://doi.org/10.1175/1520-0493(2004)132<1917:AARMMI>2.0.CO;2), 2004b.

833 Wheeler, M. C., Hendon, H. H., Cleland, S., Meinke, H., and Donald, A.: Impacts of the Madden–Julian Oscillation on
834 Australian Rainfall and Circulation, *Journal of Climate*, 22, 1482–1498, <https://doi.org/10.1175/2008JCLI2595.1>, 2009.

835 Wu, C.-H. and Hsu, H.-H.: Topographic Influence on the MJO in the Maritime Continent, *J. Clim.*, 22, 5433–5448,
836 <https://doi.org/10.1175/2009JCLI2825.1>, 2009.

837 Wu, X., Deng, L., Song, X., Vettoretti, G., Peltier, W. R., and Zhang, G. J.: Impact of a modified convective scheme on the
838 Madden-Julian Oscillation and El Niño–Southern Oscillation in a coupled climate model: MJO AND ENSO SIMULATED
839 BY A COUPLED GCM, *Geophys. Res. Lett.*, 34, <https://doi.org/10.1029/2007GL030637>, 2007.

840 Xiang, B., Zhao, M., Jiang, X., Lin, S.-J., Li, T., Fu, X., and Vecchi, G.: The 3–4-Week MJO Prediction Skill in a GFDL
841 Coupled Model, *J Climate*, 28, 5351–5364, <https://doi.org/10.1175/JCLI-D-15-0102.1>, 2015.

842 Xiang, B., Harris, L., Delworth, T. L., Wang, B., Chen, G., Chen, J.-H., Clark, S. K., Cooke, W. F., Gao, K., Huff, J. J., Jia,
843 L., Johnson, N. C., Kapnick, S. B., Lu, F., McHugh, C., Sun, Y., Tong, M., Yang, X., Zeng, F., Zhao, M., Zhou, L., and Zhou,
844 X.: S2S Prediction in GFDL SPEAR: MJO Diversity and Teleconnections, *B Am Meteorol Soc*, 103, E463–E484,
845 <https://doi.org/10.1175/BAMS-D-21-0124.1>, 2022.

846 Yang, C., Liu, J., and Xu, S.: Seasonal Arctic Sea Ice Prediction Using a Newly Developed Fully Coupled Regional Model
847 With the Assimilation of Satellite Sea Ice Observations, *J Adv Model Earth Syst*, 12, e2019MS001938,
848 <https://doi.org/10.1029/2019MS001938>, 2020.

849 Zeng, L., Bao, Q., Wu, X., He, B., Yang, J., Wang, T., Liu, Y., Wu, G., and Liu, Y.: Impacts of humidity initialization on MJO
850 prediction: A study in an operational sub-seasonal to seasonal system, *Atmospheric Research*, 294, 106946,
851 <https://doi.org/10.1016/j.atmosres.2023.106946>, 2023.

852 Zhang, C.: Madden-Julian Oscillation: MADDEN-JULIAN OSCILLATION, *Rev. Geophys.*, 43,
853 <https://doi.org/10.1029/2004RG000158>, 2005.

854 Zhou, L. and Harris, L.: Integrated Dynamics-Physics Coupling for Weather to Climate Models: GFDL SHIELD With In-Line
855 Microphysics, *Geophys. Res. Lett.*, 49, e2022GL100519, <https://doi.org/10.1029/2022GL100519>, 2022.

856 Zhou, L., Lin, S.-J., Chen, J.-H., Harris, L. M., Chen, X., and Rees, S. L.: Toward Convective-Scale Prediction within the Next
857 Generation Global Prediction System, *Bulletin of the American Meteorological Society*, 100, 1225–1243,
858 <https://doi.org/10.1175/BAMS-D-17-0246.1>, 2019.

859